Fine Pointing Assembly for Optical Ground Station

Tip-Tilt removal through feedback control

AE5810: MSc thesis - Mees Beumer

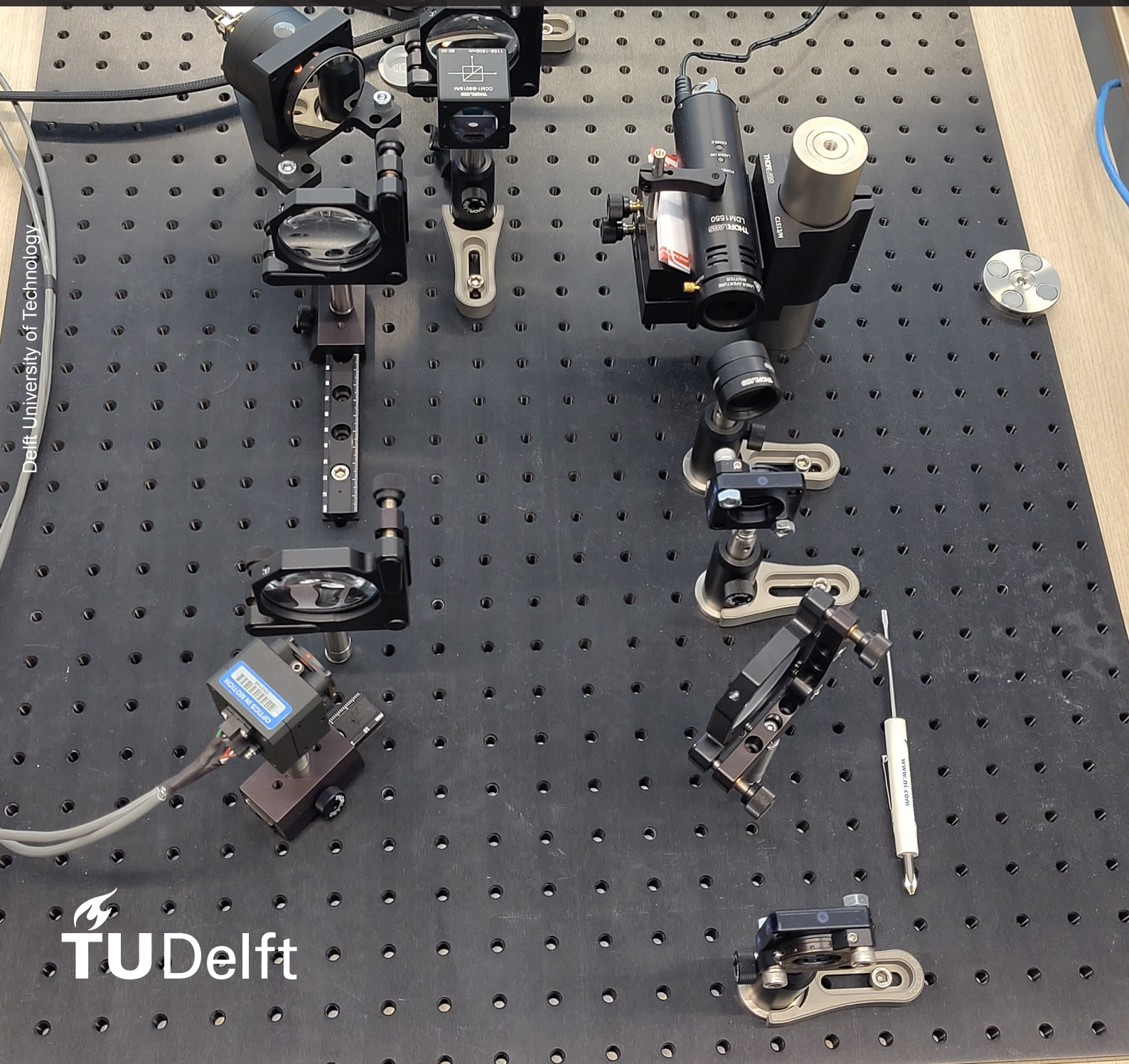

Delft University of Technology

TU Delft

Fine Pointing Assembly for Optical Ground Station

Tip-Tilt removal through feedback control

AE5810: MSc thesis

Student Name	Student Number
Mees Beumer	4648838

Institution:	Delft University of Technology	
Place:	Faculty of Aerospace Engineering, Delft	
Project Duration:	September 2023 - June 2024	
Thesis committee:	Dr. A. Menicucci	TU Delft, Committee Chair
	Dr. P. Piron	TU Delft, Examiner
	Dr.ir. R. Saathof	TU Delft, Daily Supervisor
	ir. J.J. Spaander	TU Delft, Daily Supervisor

Cover Image: Setup

TU Delft

Acknowledgement

How do you eat an elephant? Bite by bite.

This thesis was undoubtedly the most challenging thing I undertook in my career as an Aerospace Engineering student. The challenge does not limit itself to technical problems. Self-doubt, perfectionism, and decision-making. All problems I dealt with daily. But where there is a challenge, there is learning. I can say for sure that I have learned an incredible amount throughout this thesis. The learning process is what I enjoyed most, and it would not have been possible without the opportunities that crossed my path.

Thank you, Rudolf and Joshua, for answering my endless supply of questions. Thank you for your guidance and the opportunity to work with your precious hardware, for helping me cope with technical challenges and encouraging me to go the extra mile. Finalizing this thesis, I can (finally) honestly say that I'm proud of what I've made.

My gratitude extends to my friends and family. Without friendships from the Fellowkids, N.B. 2.56, AP56, SHAM SPO(R)T, and the 8th floor, I would not have been able to get this far. Rob, Godelieve, Rosemarijne, Berend, Bram, and Eleonora, thank you all for supporting me in all the ways you did. I especially appreciated your interest in my education, which, let's face it, is completely outside the medical field. It is hard to find words to tell you how grateful I am for all the opportunities you have granted me.

A special thank you to Janneke. You are always there, no matter the time or day. I reckon that now that this chapter closes, we can start a new one.

M.C. Beumer
Delft, June 2024

Summary

Over the last 40 years, the demand for internet bandwidth has increased by 50% every year [1]. Limited capacity, availability, and spectrum congestion of the RF infrastructure threaten to limit the supply of this increasing demand. Free Space Optical Communication (FSOC) in the future will supplement the RF infrastructure [2]. The Aerospace Engineering faculty of Delft - University of Technology has recently invested in developing a Mini Optical Groundstation (MISO). This lab is being built to facilitate developing and demonstrating FSOC-related technology, such as communication, laser ranging, and atmospheric studies.

MISO will consist of a 40cm telescope on top of a mount. To facilitate interfaces between MISO and commercial fiber optic equipment there is a need for a Fine Pointing Assembly (FPA). This FPA will need to reject atmospheric and vibration-induced disturbances in the received light beyond what is compensated for by the telescope mount. This thesis tackles the design task of this FPA. The design objective is formalized as follows:

Design, develop and characterize an opto-mechatronic integrated system to achieve Fine Pointing for MISO

The FPA was designed to mitigate tip-tilt disturbances as these account for roughly 80% of the variance of the total atmospheric disturbance energy [3]. The design is centered around a feedback-controlled Fine Steering Mirror (OIM102 - Optics In Motion [4] which receives feedback from a Short Wave InfraRed (SWIR) camera detector (Bobcat 320-CL - Xenics [5]) onto which the beam is projected. Digital Image Processing is performed on a separate Linux platform that runs RTMaps. The computed centroid position is then forwarded to the FPA controller run by the dSPACE- MicroLabBox. The FPA design was realized within a lab setting, shown in Figure 1.

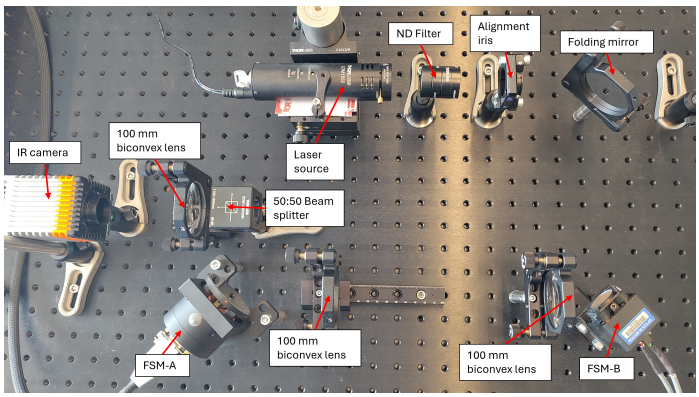

Figure 1: Optical setup of the Fine Pointing Assembly in a lab context.

After the characterization campaign, latency, as a result of digital image processing, was identified to cause large discrepancies between the desired and realized bandwidth of the FPA. Propagation of the single-sided Power Spectral Density (PSD) of the tip-tilt disturbance through the FPA indicated that 76% of the tip-tilt disturbance energy is removed.

The integrated Fine Pointing system for MISO removes part of the tip-tilt disturbance energy. However, it does not yet satisfy the system requirements related to tracking resolution and bandwidth. Recommendations for future development focus on reducing latency effects and relating the FPA system performance to the performance of MISO.

Nomenclature

Abbreviations

Abbreviation	Definition
ADC	Analog to Digital Converter
ADU	Analog to Digital Unit
AO	Adaptive Optics
API	Application Programming Interface
CMOS	Complementary Metal Oxide Semiconductor
CL	Closed-Loop
COG	Center Of Gravity
COTS	Commercial Off The Shelf
CPA	Coarse Pointing Assembly
DAC	Digital to Analog Converter
DCHP	Dynamic Host Configuration Protocol
DIP	Digital Image Processing
FIFO	First In First Out
FPA	Fine Pointing Assembly
FSM	Fine Steering Mirror
FSOC	Free Space Optical Communication
iid	Independent Identically Distributed
IoT	Internet of Things
IR	InfraRed
LAN	Local Area Network
LLN	Law of Large Numbers
LPF	Low-Pass Filter
LTI	Linear Time Invariant
MCS	MonteCarlo Simulation
MDF	Mode Field Diameter
MISO	Mini Optical Ground Station
MLBX	MicroLabBox
NA	Numerical Aperture
OGS	Optical Ground Station
OL	Open-Loop
OS	Operating System
PID	Proportional, Integral, Derivative
PSD	Power Spectral Density
QPD	Quadrant Photo-Detector
RAM	Random Access Memory
RF	Radio Frequency
RMS	Root Mean Square
ROI	Region Of Interest
ROIC CTIA	Read Out Integrated Circuit Capacitive Trans-Impedance Amplifier
RTI	Real-Time Interface
SDK	Software Development Kit
SI	System Identification
SISO	Single Input Single Output
SMF	Single Mode Fiber

SWaP	Size Weight and Power
SWIR	Short Wave InfraRed
SNR	Signal to Noise Ratio
TBF	Time Between Frames
TOI	Time Of Issue
UDP	User Datagram Protocol
ZOH	Zero-Order Hold

Symbols

Symbol	Definition	Unit
D	Aperture diameter	[cm]
f	Focal length	[m]
f_t	Tip-tilt bandwidth	[Hz]
K_i	Control gain of the Integrator	[-]
P_e	Pixel level of model with noise	[ADU]
P_i	Pixel level on pixel i	[ADU]
P_m	Pixel level of model	[ADU]
r_0	Fried parameter	[cm]
s	Pixel pitch	[m]
t_l	Latency	[s]
T_s	Sampling time	[s]
$\hat{v}$	Wind speed	[m/s]
x_i	location of pixel i on detector (x-axis)	[px]
y_i	location of pixel i on detector (y-axis)	[px]
x_{cog}	location of beam centroid on detector (x-axis)	[px]
x_{mid}	Location of frame centered coordinate system on detector	[px]
y_{cog}	location of beam centroid on detector (y-axis)	[px]
Δl	Linear displacement on detector	[m]
$\Delta\theta$	Angular displacement in optical axis	[rad]
λ	Wavelength	[nm]
μ_N	Mean background noise level	[ADU]
σ_N	Standard deviation of the background noise level	[ADU]
ω	Beam radius at the detector	[px]

Contents

1 Introduction

For four decades, Internet consumption has increased bandwidth requirements by 50%[1] each year. As of 2024, the average consumer bandwidth is above 1 Gbps. By 2030, Nielsen's law of internet bandwidth predicts to supersede 2 Tbps. This higher demand can be explained by emerging technologies that produce and consume increasing amounts of data. Some examples of these technologies are the Internet of things (IoT), Self-driving cars, etc. Simultaneously, there are emerging desires for global connectivity, high-volume data transfer, and data security [6].
Although the Internet is provided mainly by terrestrial networks, Internet connectivity from space is becoming more accessible [7],[8],[9]. Radio-frequency (RF) technology currently serves as the main method to transfer data between ground and orbit. Spectrum congestion and limited available bandwidth threaten to limit the supply of these increasing bandwidth demands [2].
Free space optical communication (FSOC) technology will service this new demand by complementing the RF and terrestrial Internet infrastructure [2].

The faculty of Aerospace Engineering (TU-Delft) has recently invested various funds to develop a mini optical ground station (MISO)[10]. MISO is intended as a laboratory to test and demonstrate FSOC-related technology such as laser ranging, ground-to-space optical communication, and atmospheric research.

At its heart, MISO will consist of a 40 cm telescope Alluna Ritchey-Chrétien telescope [11] mounted on a PlaneWave L-500 Direct Drive Mount[12]. A photo of the telescope assembly of MISO alongside a schematic is shown in Figure 1.1.

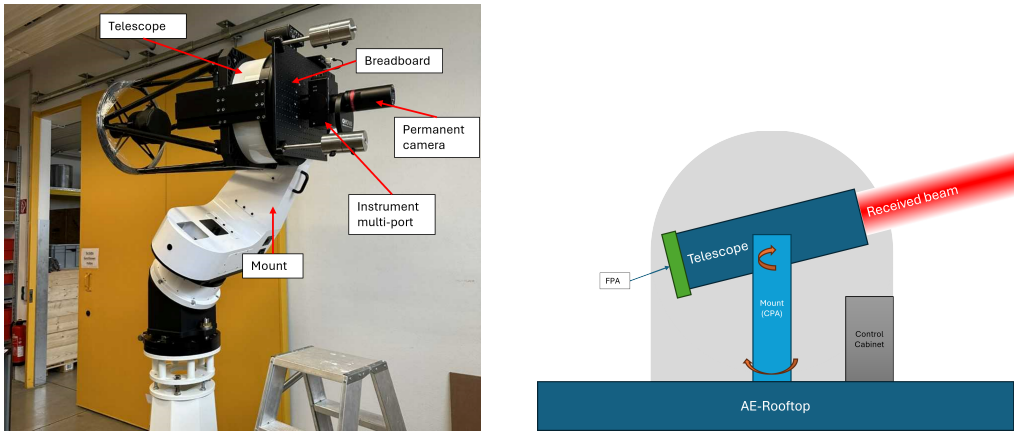

(a) MISO telescope assembly assembled by manufacturer. **(b)** Concept sketch of MISO.

Figure 1.1: MISO concept visualized.

FSOC terminals partaking in space-to-ground links are subject to stringent link budgets due to the lower divergence compared to RF communication technology [2]. In these budgets, geometric and atmospheric losses are among the main contributors [13]. As a satellite moves over the optical ground station, its elevation angle changes, thereby passing through different paths in the atmosphere with different lengths. Link budgets, therefore, are partly driven by path length through the atmosphere. This translates to the minimum elevation angle required for a closing link budget for a ground station. Elevation angles commonly used for FSOC links are in the range of roughly $30° < \theta_{elevation} < 150°$ [14]. Note that this is a rough estimate. The minimum elevation angles are specific to the system architecture and selected components. Besides this large field of regard, FSOC terminals must simultaneously provide μrad accuracy.

Since fiber optic communication is considered a mature technology, the received light is often coupled into a single-mode fiber (SMF) to perform data detection, etc., on commercial off the shelf (COTS) equipment [2]. Coupling into SMF requires a better pointing performance than the telescope PlaneWave system alone. Therefore, the pointing functionality is separated between two systems. The large range and slow pointing are achieved by the coarse pointing assembly (CPA), while the smaller range and fast motion are done using a fine pointing assembly (FPA) [15] [16]. Figure 1.1 shows where these systems (will) reside within MISO.

1.1.The Fine Pointing Assembly

MISO, when used as a receiving optical terminal, will use optical fiber technology as a baseline for data detection, in the future free space coherent detection is envisioned[1]. Facilitating coupling into SMF imposes the strictest pointing requirements on MISO beyond the performance of the telescope mount, the CPA. This thesis will focus on designing, developing, and characterizing an FPA for MISO to facilitate the optical path between the telescope and SMF. The context of this FPA is presented in Figure 1.2.

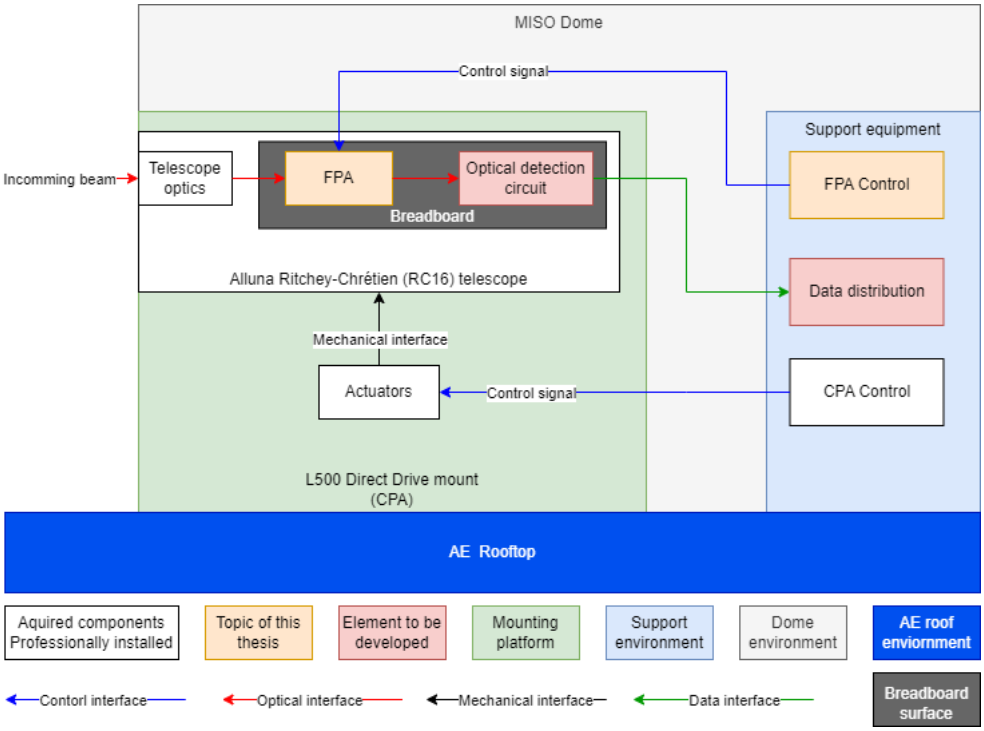

Figure 1.2: Context diagram of the FPA

MISO will feature a breadboard mounted on the focal plane of the telescope, shown in Figure 1.1.a. The FPA will, in the future, be installed here.

A challenge for the design of the FPA is the schedule. As of the start of this thesis, MISO has not yet been built. The same applies to the environment in which the FPA has to operate. For this reason, literature and heritage were consulted, the latter presented in Table 1.1.

[1] Internal communication

Ground Station	location	Residual pointing error [μrad]	operational?	Fine pointing	Feedback sensor	Source
OCTL	Wrightwood	9.7	Y	Deformable mirror	Shack-Hartmann wavefront sensor (Xenics Cheetah)	[17]
DSS-13	Goldstone	<1	Y	FSM (piezoelectric)	Photon counting camera	[18]
Unknown	Nemea	<24.2	Y	Unknown	Unknown	[19]
Unknown	Almeria	<48.5	Y	Unknown	Unknown	[19]
El Teide	Tenerife	<+-500	Y	Voice Coil Deformable Mirror (AO)	Shack-Hartmann wavefront sensor	[19] [20]
NICT-OGS	Tokyo	39.2	Y	Fine pointing mechanism	Quadrant detector	[21]
OGS-OP	Oberpfaffenhofen	unknown	Y	FSM	NFOV camera (near infrared)	[22]
TOGS	N.A.	TBD	Planned	Not present	NFOV camera (near infrared)	[22]
AOGSN	Network, various locations	TBD	Planned	Deformable mirror (AO)	Shack-Hartmann wavefront sensor	[23]
Unknown	El Segundo (US)	40	Y	Not present	Xenics InGaAs camera array	[24]

Table 1.1: Heritage database of OGS across the world (as of April 2024)

1.2.Requirement generation

To be compatible with MISO, several customer and system requirements are imposed on the design and implementation of the FPA. These are presented in Table 1.2, 1.3.

The customer requirements were established together with the future operators of MISO. The system requirements are derived from literature and the heritage in Table 1.1. The motivation for each of these requirements is presented below. Notably, these requirements will need further verification once MISO is operable. This is touched upon in Section 3.2

Label	Parent	Child requirement	Motivation
FPA1-1	The FPA shall only use hardware and software components made available through the Space System Engineering department as of October 2023.		Most of the investments were already made by the SSE department to acquire ”long lead items” early on.
FPA1-1A		The FPA shall be prototyped in a lab environment, only demonstrating and characterizing its performance	This requirement limits the scope of this thesis.
FPA1-1B		The FPA shall make use of Digital Image Processing.	Desired capability by the LaserSatCom research group.
FPA1-2	The FPA shall be modular in design.		Ease of further development. Modularity will allow for upgrades on specific elements in the FPA.

Table 1.2: Customer requirements for MISO FPA related to this thesis.

The role of the FPA within MISO is to bridge the gap between the telescope and an SMF used to receive a downlink from a satellite in low earth orbit. To this end, the top-level system requirement is formulated as:

FPA1-3:*The FPA shall facilitate coupling of the received laser beam from the CPA into an SMF.*

System requirements flowing down from this requirement are presented in Table 1.3 and further elaborated upon below.

Label	Parent	Child requirement	child of child
FPA1-3	The FPA shall facilitate coupling the received laser beam from the CPA into an SMF.		
FPA1-3-1		The FPA shall reduce Tip-tilt disturbance in the received laser beam	
FPA1-3-1A			The FPA shall have a gain crossover bandwidth of >100 Hz with the desire of >1000Hz.
FPA1-3-1B			The FPA shall reduce the total disturbance energy in the measurable Tip-tilt PSD of the incoming beam.
FPA1-3-2		The FPA shall have a tracking resolution of $\leq 5\mu rad.$	
FPA1-3-3		The FPA shall have an angular acceptance range of $\pm 500\mu rad.$	

Table 1.3: System requirements for MISO FPA related to this thesis.

Tip-Tilt removal (FPA1-3-1)
Upon arrival, the laser traveling through the atmosphere has a distinct phase profile that can be decomposed into a linear combination of Zernike polynomials [25, p.24]. Figure 1.3 shows spread in the residual pointing error after specified modes of the Zernike polynomials are removed from the beam [3, Table. 4].

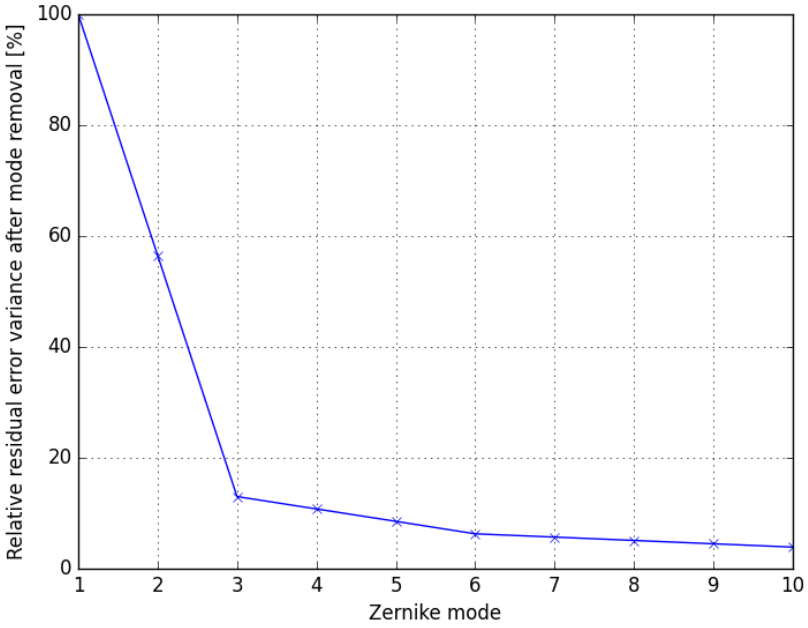

Figure 1.3: Relative residual error variance in Kolmogorov turbulence after removal of Zernike modes [3].

Fully removing just the Zernike modes 2 and 3, tip and tilt, respectively, the remaining mean residual error is reduced to 13% of its original value. Mitigating beyond tip-tilt correction is considered not cost effective in terms of both complexity and financial cost[2] hence the FPA designed in this thesis will only remove tip and tilt.

An adaptation of Tyler's turbulence tracking bandwidth is given by Equation 1.1 [26]. This model assumes only a single dominant layer of wind speed $\hat{v}$. Most of the disturbance energy originates in the lower part of the atmosphere and is quite large compared to the angular motion of a satellite in orbit[26]. For MISO, the wind speed is assumed to be $20m/s$.

$$f_t = 1.62\hat{v}/D \tag{1.1}$$

The bandwidth requirement for the FPA (**FPA1-3-1A**) is computed to be $81Hz$. However, it was raised to $100Hz$ to maintain some performance margin.

Atmospheric tip-tilt, although dominant, is not the only disturbance to be mitigated. Micro-vibrations on satellite and ground stations are still present, leading up to $1kHz$ [15, Fig.5]. A bandwidth $> 1kHz$ is therefore desirable.

The Glindemann single sided power spectral density (PSD) given by Equation 1.2 and 1.3 [26] indicate the tip-tilt disturbance energy in the beam before either tip or tilt is removed, each for their respective axis. The FPA shall act as a high pass filter, attenuating the tip-tilt disturbance. The total remaining energy of the altered PSD can be compared against the original PSD to understand the amount of disturbance energy removed from the beam using the FPA **(FPA1-3-1B)**. The PSD is generated with

[2] Conversation with the customer

the parameters shown in Table 1.4, note that the model requires the seeing ($\lambda 0$)in arcseconds. The input PSD displayed changed to rad^2/Hz can be seen in Figure 3.7.

$$P_{f_{low}}(f) = 0.096(r_0/\hat{v})^{1/3}(\lambda/r_0)^2 f^{-2/3} \quad [arcsec^2/Hz] \tag{1.2}$$

$$P_{f_{high}}(f) = 0.0013(D/\hat{v})^{-8/3}(\lambda/r_0)^2(D/r_0)^{-1/3} f^{-2/3} \quad [arcsec^2/Hz] \tag{1.3}$$

Parameter	Description	Value	Unit
r_0	Fried parameter	19	cm
$\hat{v}$	Wind speed	20	m/s
λ	Wavelength	1550	nm
D	Aperture diameter	40	cm

Table 1.4: PSD input parameters

Tracking (FPA1-3-2)
To facilitate coupling the beam exiting the FPA into a SMF, in a lab environment (**FPA1-1A**) with Gaussian beams, the FPA shall be able to focus the profile into the mode field diameter (MFD) [27, p.20], which for a SMF is $10.4\mu m$ wide [27, p.36].

It is assumed for the generation of this requirement that the FPA removes all tip-tilt disturbance energy, which is the only disturbance present within the lab environment. Then, the requirement becomes a static pointing problem. As a conservative estimate the beam waist at the SMF is sized to $4\mu m$ which leaves $1\mu m$ margin on either side in the mode field. Having a smaller beam waist than half the MFD reduces the coupling efficiently by ≈ 7% [27, p.22], however, does allow for slight pointing errors.

Gaussian beam propagation of a $3mm$ diameter beam collimated beam diameter yields $12mm$ focal distance of focusing lens. This is close to the recommended $15.8mm$ lens prescribed by Thorlabs [27, p.24]. For a max error of $83.3\mu rad$, the beam will still be fully inside MDF. As a conservative estimate, the tracking resolution should be 10x better than the maximum allowable pointing error.

With this line of reasoning, the pointing resolution requirement was sized to be $5\mu rad$. **(FPA1-3-2)**. This order of magnitude in tracking resolution is corroborated by KODEN its performance [28, Fig 6.d], where a similar tracking resolution is shown. It should be noted that a tracking resolution requirement based on allowable fade rate and duration would be less conservative.

The tracking resolution will in the future dictate the required optical power for tracking, therefore this separate requirement was removed. A pointing resolution requirement was also no longer included as the feedback system of the FPA cannot achieve better pointing than it can track.

FPA angular domain (FPA1-3-3)
The angular acceptance range of the FPA heavily depends on the CPA performance, in the case of MISO, the Plane Wave l500 mount. Information on its performance is limited. Therefore, conservative numbers were used.

The l500 mount is rated to have 10" RMS accuracy below $10Hz$ [12]. However, better pointing accuracy has been shown using PointXP models on slow-moving objects, like LEO satellites [29]. In the remainder of this thesis, the CPA is considered a High-pass filter with a cut-off frequency of $10Hz$. At frequencies beyond $10Hz$, the pointing error is 10" RMS.

For the FPA design process, the worst-case pointing error was used to size the minimum angular acceptance. On a periodic motion, 10" RMS is roughly $100\mu rad$ peak-to-peak. Applying a conservative factor of 10 requires the FPA to have an angular acceptance range of $\pm 500\mu rad$ **(FPA1-3-3)**. This range is comparable with what can be found in literature [16][28].

1.3.Thesis objective & report outline

The research objective for this thesis was formulated based on the context and the customer and system requirements presented in Table 1.2 and 1.3, respectively.

Objective:
Design, develop and characterize an opto-mechatronic integrated system to achieve Fine Pointing for MISO

The report supporting this thesis objective is structured as described by Figure 1.4. Chapter 4 introduced the context of this thesis and the requirements. In Chapter 2a functional analysis is performed, motivating the chosen topology and component selection. Afterwards the system-level design and the implementation and characterization strategies are addressed. Chapter 3 introduces the results in terms as a result of the various characterization campaigns. Additionally, in this chapter, the FPA and the design process are critically reflected upon. Lastly, Chapter 4 formulates the conclusion of the development of the FPA using compliance matrices while also presenting the main insights obtained through this thesis. Several recommendations for future development will be given.

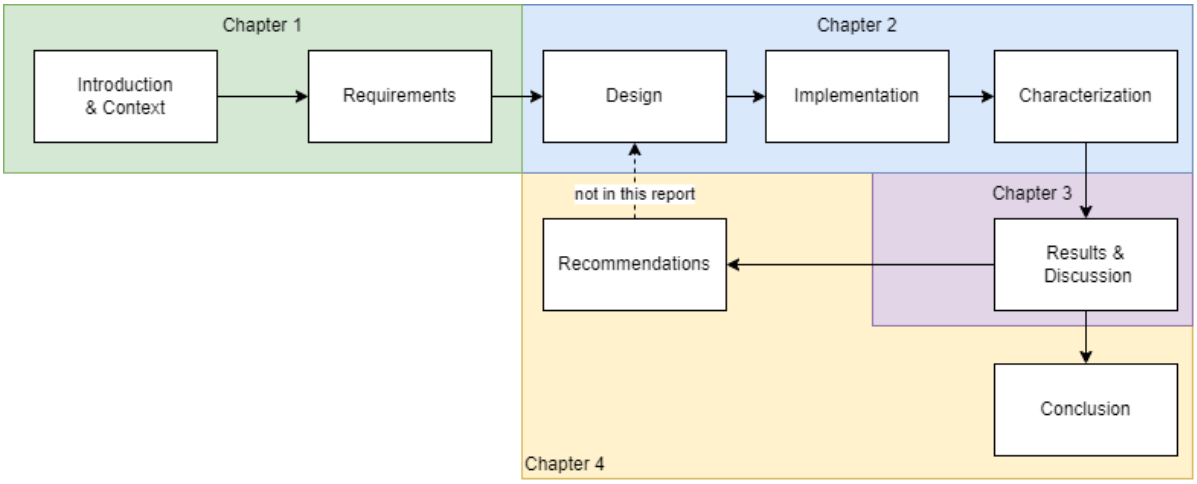

Figure 1.4: Report outline of this thesis

2
Design, Implementation & Characterisation

The design objective and requirements established in Chapter 1 are translated into a design in this chapter. This is done by first performing a functional analysis and subsequent component selection Section 2.1.1. The components their interfaces are compiled into a system design in Section 2.1.3. Integration activities start with the commissioning of the individual components in Section 2.2.1, followed by an optical design in Section 2.2.3, digital image processing toolchain in Section 2.2.2, and finally implementation of a control system in Section 2.2.4. This chapter ends with an explanation of the characterisation strategies for the different domains of the FPA.

2.1.Design

Before the design is introduced, the working principle of the FPA will be introduced, motivating several design choices later. Afterward, components are selected, and a system-level design is drafted.

2.1.1. Functional analysis

As described in Section 1.1, the FPA reduces the tip-tilt disturbance energy present in the received beam from the CPA. This stabilized beam is intended to be coupled into an SMF detection circuit (not part of this thesis).

The FPA design intends to mitigate only the tip-tilt pointing errors by introducing equal but opposite angular displacements utilizing beam steering into the local path of the incoming beam. The resulting beam is actively being pointed towards the center of the mode field of the SMF. This corresponds to the setpoint of the feedback control system, facilitating the fiber coupling efforts by the detection circuit. Figure 2.1 shows the functional flow diagram associated with the FPA designed for MISO.

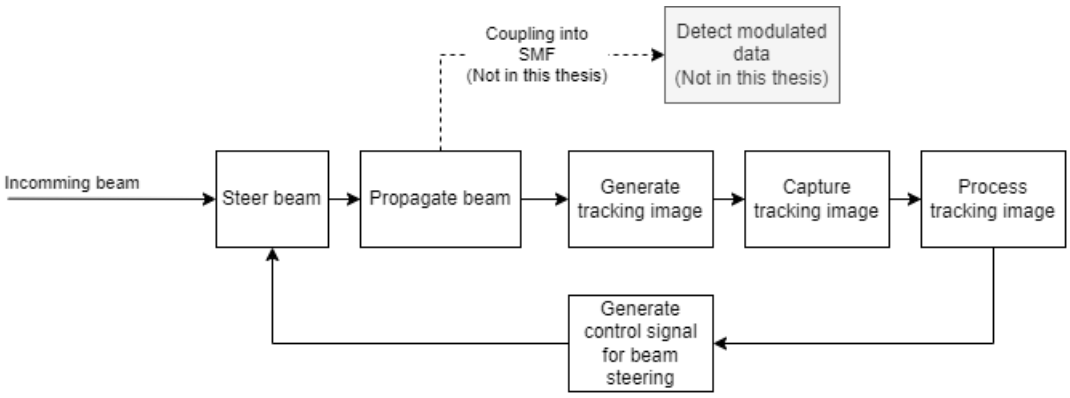

Figure 2.1: Functional flow diagram of FPA designed for MISO.

The disturbed beam is projected onto a tracking sensor. The beam location is computed from the image. The beam forms the feedback signal to the controller, which generates the command signal to move the beam to the desired location.

2.1.2. Component selection

Component selection for the FPA was made based and limited to functionality and customer requirements **FPA1-1** and **FPA1-1B**.

As mentioned inSection 1.2 and 2.1.1, the FPA will only remove tip-tilt errors from the incoming beam. Heritage, Table 1.1, shows most optical ground stations (OGS) use adaptive optics (AO). Although this fine pointing mechanism performs better regarding residual disturbance energy, it is much more complicated and costly while only marginally improving the performance compared to tip-tilt removal using a 2 axis fine steering mirror (FSM). The customer has expressed these costs do not outweigh the benefits of implementing AO [1].

Analyzing FSOC receiving terminals on satellite platforms Table D.1, it becomes clear that a similar trade-off is made for the more compact terminals onboard satellites. For these platforms, the AO solution is too costly in terms of size, weight, and power (SWaP), but also complexity and reliability

MISO as a laboratory is intended to provide insight into beam interactions with the atmosphere. To this end, digital image processing (DIP) is desired by the customer (**FPA1-1B**). In contrast to quadrant photo-detectors (QPD), DIP provides visual access to the beam intensity profile. Additionally, DIP allows for a more versatile palette of tracking algorithms to be developed and implemented using the same FPA architecture.
Lastly, the component selection was also based on the functional flow diagram Figure 2.1 and the associated functional analysis shown in Table 2.1 along with the selected components. Design Option Trees for each of the functionalities are presented in Appendix B, and the specifications of the selected components can be retrieved in Appendix C.

Adhering to the lab demonstration requirement (**FPA1-1A**), a second FSM is included in the lab setup. This extra mirror introduces a tip-tilt disturbance into the undisturbed beam.

Function	Description	Selected component
FPA		
Propagate beam	Beam is guided through the FPA with the use of transmissive optics	Various bulk optics - Thorlabs
Steer incoming beam	2 axes voice coil actuated flat 2” mirror	OIM 102 & OIM100 - Optics In Motion
Track beam projection	CMOS SWIR camera taking image of beam projection	Bobcat 320-CL - Xenics
Capture tracking images	Frame grabber to record frames generated by the camera and make available for processing in local OS RAM	Grablink Full - Euresys
Process tracking images	Near Real-time modular processing capability	Lenovo ThinkStation P620 (Linux PC) & RTMaps - Intempora
Generate control signal for beam steering	Receive feedback signal and generate control signals based on setpoint and feedback	MicroLabBox (rti1201)(MLBX) - dSPACE
Support equipment for lab demonstration and testing		
Generate beam	Laser Diode emitting collimated beam of $1550nm$	LDM1550 - Thorlabs
Propagate beam	beam is guided through the FPA with the use of transmissive & reflective optics	Various bulk optics - Thorlabs
Emulate angular beam disturbance	2 axes voice coil actuated flat 1” mirror	OIM5001 & OIMC_A - Optics In Motion
Provide power to FSM-B controller	Provide $\pm 15V$ to OIMC_A controller	Keithley 2200G-30-1

Table 2.1: Functional analysis of processes in the FPA as described in Figure 2.1.

[1] Internal communication

2.1.3. System level design

Referring back to the functional analysis and the component selection, further analysis of the infrared (IR) camera shows that two coordinates describe centroid tracking of the beam as the image uses a 2D Cartesian coordinate system. This allows the FPA to operate using two uncoupled feedback signals.

When used with its internal PID controller from Optics In Motion in place, FSM-A is assumed to act as two parallel single-input-single-output (SISO) linear time-invariant plants. This assumption will be verified in Chapter 3.

All functionalities from Figure 2.1 can be executed in an uncoupled fashion. Therefore, the FPA was designed as two parallel SISO control systems.

The FPA architecture is shown in Figure 2.2 and features interfaces shown in Table 2.2.

Interface	Implementation strategy	Availability
Optical	Placement of bulk optics	Commercial product
Camera-to-Grablink full	Install CameraLink video cable between IR camera and frame grabber	Commercial product
Grablink full-to-RTMAPS	Program C++ component for RTMaps to interact with frame grabber using Multicam driver API	Self-made software
RTMaps-to-MLBX	Integrate dSPACE toolchain between RTMaps and Simulink RTI Ethernet blockset	Commercial product
MLBX-to-MLBX	Set-up controller that can be interacted with through ControlDesk, generate control signal based on feedback and set-point	Self-made software
MLBX-to-FSM	Attach BNC cables to DAC and ADC connectors on MLBX and connect to corresponding command and position connectors on FSM controllers (OIM100 and OIMC_A)	Commercial product

Table 2.2: Interfaces present in the FPA setup, including their respective implementation strategies.

Modularity within the design

Modularity within the design of the FPA as dictated by the customer **(FPA1-2)** fits with the purpose of MISO as a technology demonstrator and research platform. The modular design of the FPA enables research with MISO on a specific element without considering the whole architecture.

Modularity is achieved by separating sections of the system in both hardware and software domains. Using standardized hand-overs such as the IplImage format, voltage signals $\pm 10V$, and data transfer in radians enable operators to switch hardware and software without the need for elaborate new interfacing efforts. With this strategy, the elements of this design remain transparent and interchangeable.

For example, keeping data transfer in radians removes the need for unit conversion within the gains of the control system. When a component changes in implementation while still outputting the data in radians, the control gains do not need re-tuning.

Another example is when a new tracking algorithm is desired. The operator only has to put in IplImage and output radians. This specific example is further discussed in Section 3.2

Within the design of the FPA, several modules can be identified: Optical design, FSM, IR camera, Frame size, Tracking algorithm, control layout, and gains. Most of these modules, as long as they respect the standardized interface hand-overs, can be considered ”plug & play”.

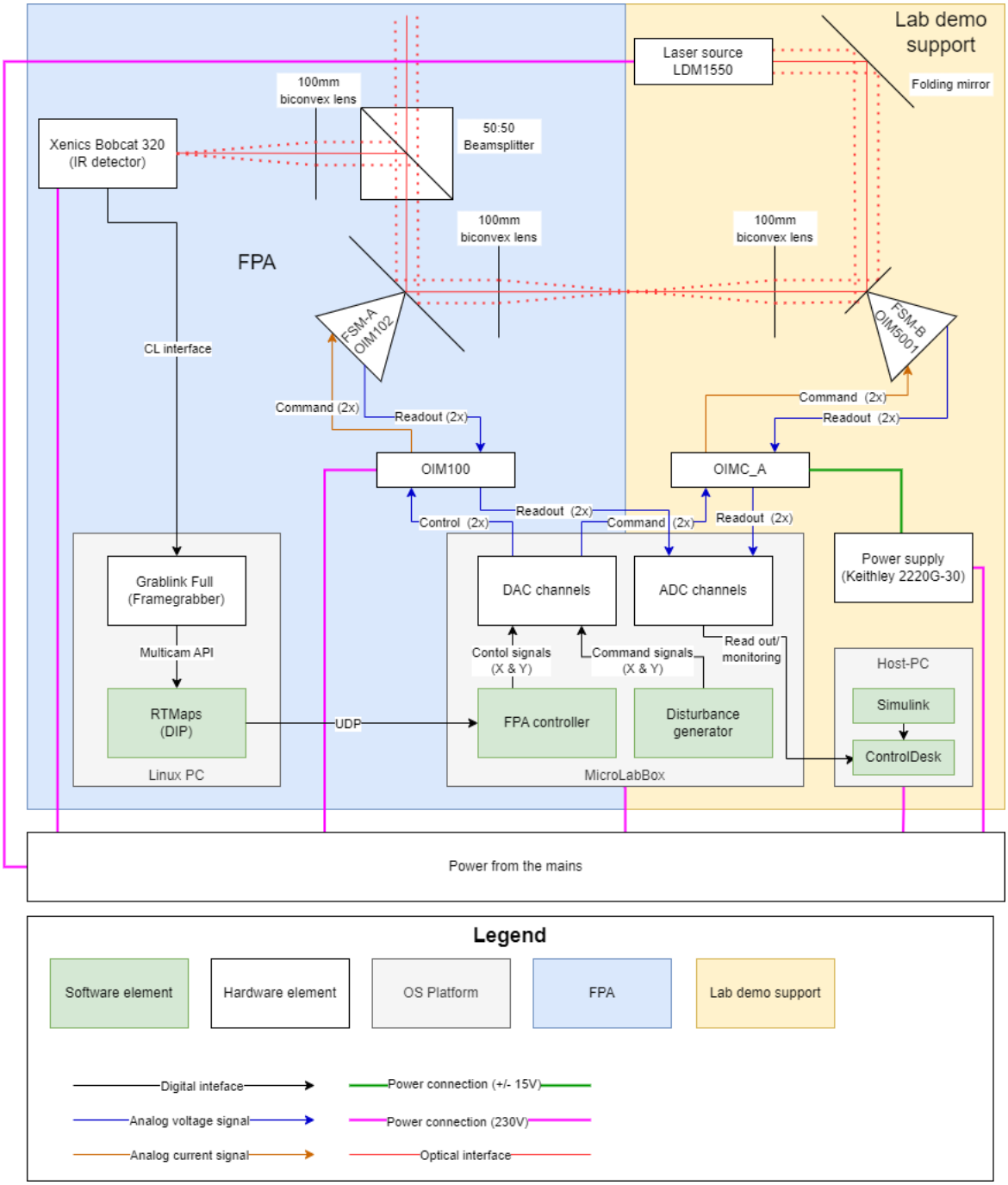

Figure 2.2: Lab experiment schematic.

2.2.System integration

This section is dedicated to the implementation of the above design. The optical design, Digital Image Processing, and control system will be reviewed.

2.2.1. Commissioning

The commissioning phase of the integration is focused at controlling each of the hardware components individually. The hardware components considered are MLBX, two FSMs, and the IR camera.

Network

A local area network (LAN) is the main interface of the FPA. The MLBX, operated through Host PC with dSPACE ControlDesk, introduces the need for a LAN connection. Additionally, the LAN supports the user datagram protocol (UDP) interface between RTMaps and the MLBX, which will later be used to transfer the coordinates of the beam center to the MLBX. All clients within the LAN have a static IP address. Clients within the LAN are the Host PC, the Linux PC running RTMaps, and the MLBX. The MLBX is assigned two addresses, one for the Host PC and the other for the UDP interface with Linux.

Commissioning the MLBX from within ControlDesk is achieved by setting up a static IP address on the Host PC, different than the one from the MLBX, and registration of the MLBX within ControlDesk [30].

The UDP connection between MLBX and Linux PC is setup up with a combination of the RTI Ethernet blockset, not the UDP blockset as this is incomparable with the MLBX and the RTMaps Interface Blockset. The interface requires the generation of a MatLab bus, which eventually formats the data leaving the RTMaps environment in a UDP package through the transfer of the XML file. The IP address and port are selected in both RTMaps and Simulink. Note that a different IP address and port than the Host PC connection must be used.

The network architecture for the FPA is shown in Figure 2.3. The IP addresses and port numbers are free to be selected as long as they differ and follow the 192.168.140.x format.

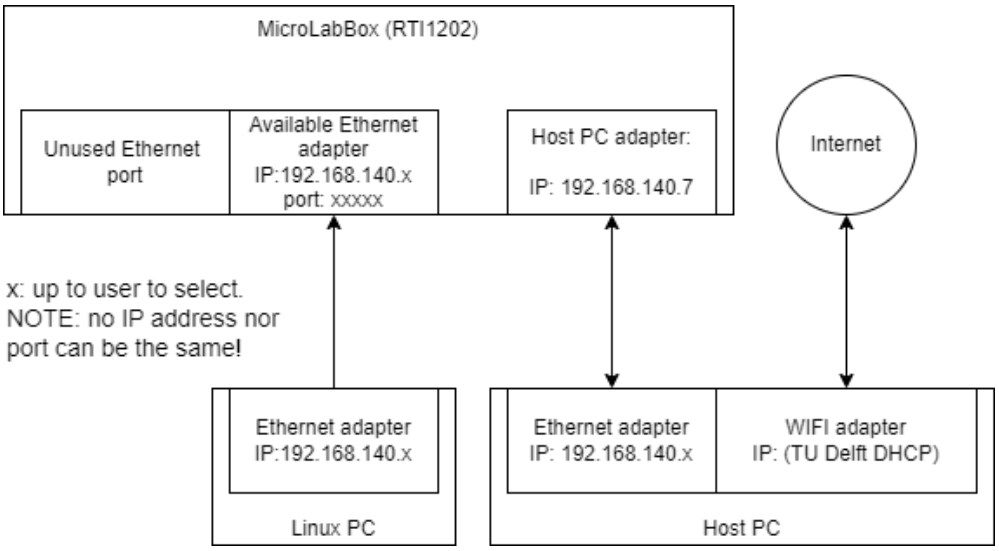

Figure 2.3: Network architecture of the FPA setup.

The MLBX could theoretically be directly wired up to the TU Delft network and can act as a network switch for the attached Linux and Host PC. Unfortunately, this requires the MAC address to be recognized and registered in the TU Delft network. Additionally, the dynamic host configuration protocol (DCHP) server of the TU Delft network determines which IP address is carried by which platform, and this might change within a single day. The network is local and isolated from the Internet for the above reasons. The Host PC, however, can access the Internet through a separate WIFI dongle, using two network adapters.

FSM-A (OIM102)
The OIM102, FSM-A, was selected as the beam steering method within the FPA because of its availability (**FPA1-1**), ease of implementation, and dynamic behavior. This FSM has the lowest bandwidth compared to the FSMs available. Selecting it for the FPA ensured the full relevant spectrum could be measured.

The OIM102 is a 2” suspended mirror that is actuated by voice-coil pairs in a push-pull configuration for the two orthogonal X and Y axes. The mirror is controlled by the OIM100 controller, which, in stock form, has two functionalities. These are voltage-to-current amplification and feedback control based on mirror position. The FSM its mirror position is commanded with analog voltage signals within the $\pm 10V$ range, corresponding to $\pm 1.5°$ of mechanical motion. These signals are realized by commanding two 16-bit digital-to-analog converter (DAC) channels on the MLBX. The mirror head position, used for internal feedback, is also available to the operator and is provided as a $\pm 10V$ analog signal. Two 16-bit analog-to-digital (ADC) channels on the MLBX sample the mirror position [31].

The internal PID controller of the OIM100 controller ideally is not included in the FPA. In system identification (SI) campaigns, the PID controller is shown to have a crossover bandwidth of roughly $250Hz$, which is lower than the desired bandwidth of $1kHz$ (**FPA1-3-1A**). Additionally, the internal PID controller frustrates the application of rules of thumb related to loop shaping methods of 2nd order mass-spring-damper systems [32, p.281], further discussed in Section 2.2.4.

As mitigation of technical and schedule risks, a switch was added to the OIM100 to keep the internal PID functionality optional. The schematic is presented in Figure 2.4.

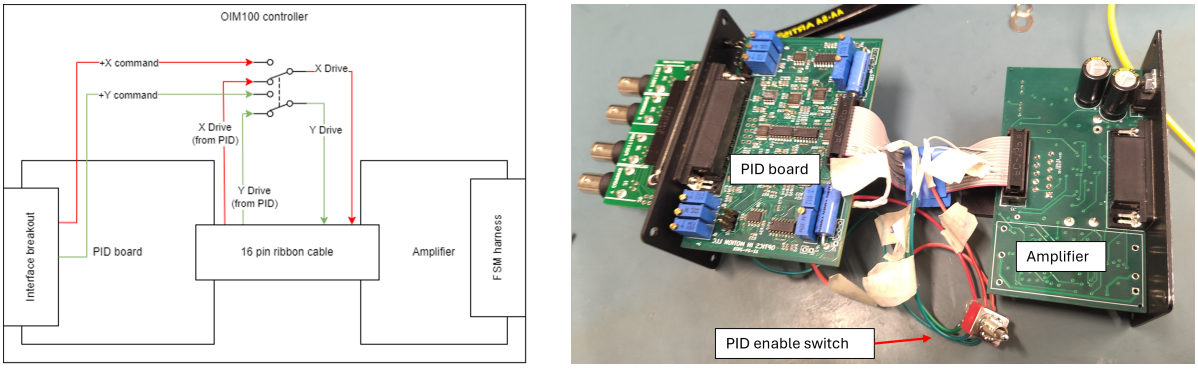

Figure 2.4: Schematic of OIM100 controller with the PID switch (left). Photo of implementation (right)

On first inspection, the removal seemed successful. The mirror head was no longer responding to angular disturbances in its position, indicating that the feedback control loop was interrupted. However, with this interrupted PID controller, the mirror proved difficult to control in open loop.

Railing was observed for signals with amplitudes of $< 0.1V$. Railing is the term used by Optics In Motion for the mirror head hitting the housing beyond the rated mechanical range of motion. The amplifier accepts significantly smaller amplitude input signals, usually scaled down by the gains of the PID controller when enabled. Next to railing, also hysteresis effects were observed noticed when sweeping command voltage levels. Upon revisiting a voltage level, different mirror positions were measured. Finally, the axes of the FSM were no longer fully uncoupled.

The above observations made it difficult to perform SI and, therefore, to model the FSM as two uncoupled LTI 2nd-order mass-spring-damper systems.

The process of removing the PID controller was paused because of schedule risk. In the remainder of this thesis, the OIM100 is always used with internal PID functional.

FSM-B (OIM5001)
The OIM5001, FSM-B, introduces tip-tilt disturbances into the laser beam before entering the FPA. The choice to designate this FSM to the support hardware is motivated by two reasons. The working principle of this 1" FSM is similar to FSM-A at a smaller form factor. This mirror is controlled by the OIMC_A, a more compact and integrated version of the OIM100. This controller provides only proportional feedback control. Because the OIMC_A is a single PCB, the controller is more difficult to isolate and disable than the OIM100. Additionally, as already briefly mentioned, this FSM has a higher bandwidth than OIM102 [4] [33], useful for SI over the full relevant spectrum of the FPA. For the above two reasons, the OIMC_A controller and OIM5001 FSM are used as support hardware to facilitate the lab demonstration (**FPA1-1A**).

To operate FSM-B, custom harnesses for both power supply and control were required. The OIMC_A requires $\pm 15V$ at a maximum of $1.5A$, a ground reference, and earth ground [34]. The Keithley 2220G-30-1 DC power supply was configured to track its two channels and was wired up as shown in Figure 2.5 [35, p.25 Fig. 5]. The interface harness breaks out the command and position signals to and from the MLBX for both axes.

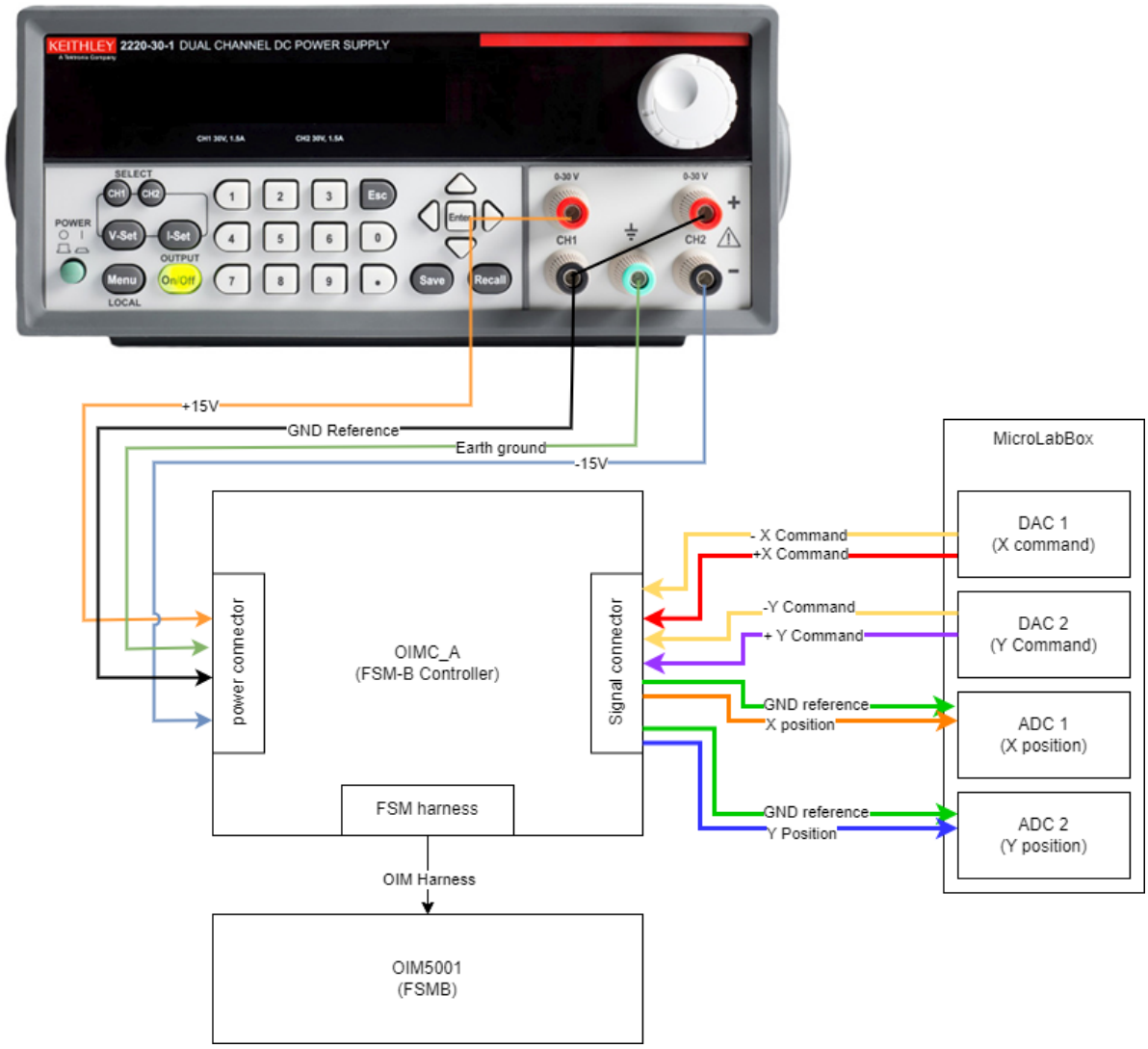

Figure 2.5: OIMC-A Interface diagram with MicroLabBox and Keithley 2220G-30-1.

IR Camera - Bobcat 320-CL
The requirement to use DIP (**FPA1-1-B**) along with the availability of components (**FPA1-1**) lead to the use of the Bobcat 320-CL. Selecting this camera implied that the DIP toolchain was to be made outside the Simulink MLBX environment as the MLBX is not compatible with CameraLink[36], the digital data transfer protocol of the IR camera. The FPA design accounts for this interface mismatch by taking the DIP toolchain outside the MLBX, housing it on the Linux PC, and supplying the coordinates of the angular displacements to the MLBX over a UDP interface.

The IR camera interfaces with the Linux PC over CameraLink, for which a frame grabber Grablink Full[37] was installed. MultiCam, the driver for the Euresys frame grabber, governs the CameraLink interface. The operator interacts with the camera using the MultiCam application programmable interface (API) or the Xeneth software supplied by Xenics. Unfortunately, the Xeneth software is only compatible with Windows. For this reason, the camera was configured once, after which the frame grabber was migrated to the Linux PC. Note that settings can also be adjusted in the operational FPA by altering the CAM file or MultiCam API. Upon every start-up, the camera retrieves the settings stored in its local memory. The configured settings turned off all automatic gain control, histogram correction, etc. Also, the exposure was set to $1\mu s$. 15 minutes after start-up the camera reaches a stable temperature. These are the operational conditions used in the rest of the thesis.

For the operation of the FPA, the CameraLink is set up between the IR camera and Linux PC. The application RTMaps[38] interacts with the MultiCam API to retrieve the captured frames. MultiCam configures a channel and sends one trigger to start the capture of frames. The IR Camera, from this point on, times its exposures readout, etc., to maintain the specified frame rate. More details on MultiCam interaction are shared in the DIP section, Section 2.2.2.

2.2.2. Digital image processing

The DIP toolchain, as seen in Figure 2.2, records and provides the feedback signals of both X and Y angular deflection. The toolchain resides mostly in RTMaps and is on the Linux PC hosting the frame grabber.

RTMaps is a software platform that supports the parallel operation of so-called components. These are blocks of code, each operating at their respective maximum speed while taking care of the first-in-first-out (FIFO) buffers between asynchronous components. Many components are supplied, but using the Software Development Kit (SDK), custom components were developed in C++ to extend the functionality of the platform. RTMaps allows for modular upgrades of the DIP toolchain, thereby adhering to customer requirement **FPA1-2**.

The DIP toolchain uses mainly custom components, except for the dSPACE UDP pipeline. Figure 2.6 indicates how the captured image traverses the DIP toolchain.

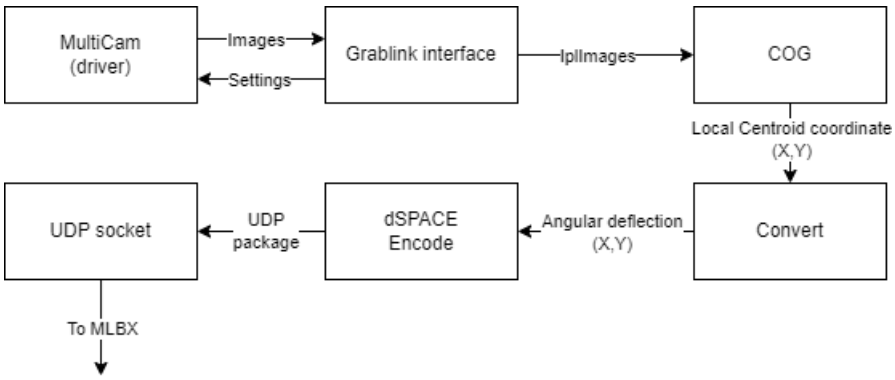

Figure 2.6: Flow chart of DIP toolchain.

The developed components are introduced in Table 2.3. The custom components are further explained below.

Component	Description	Custom or Off the shelf
Grablink interface	Component interact with MultiCam driver to configure the frame grabber and camera. After start-up the component copies frames into IplImage format to the local RAM.	Custom
COG	Retrieve IplImage from RAM and apply COG algorithm to find the local x and y coordinate of the centroid. This centroid corresponds to the peak intensity of the observed beam.	Custom
Convert	Converts the local x and y coordinates of the centroid (in pixels) to angular displacement within the FPA coordinate system.	Custom
dSPACE encode	Encodes the centroid coordinate into a UDP package formatted using RTMaps components in Simulink library	Off the shelf
UDP socket	Sends the received UDP package over the LAN to the designated socket	Off the shelf

Table 2.3: Description of the RTMaps components shown in Figure 2.6.

Grablink interface component
RTMaps components are divided into three sections: birth, core, and death [39]. The Grablink custom component was developed to suit these phases.

At birth, the MultiCam driver configures the frame grabber with the camera settings provided by the CAM file. MultiCam is commanded to open a channel in which surfaces, the image captured, will be stored and moved into RAM. The transfer of newly arrived surfaces is managed by MultiCam by the assignment of the custom callback function.

In the core of the RTMaps component no processes take place as the callback is executed outside of the RTMaps environment and is fully controlled by the MultiCam driver.

The callback function is called each time a new surface arrives in the frame grabber. The camera triggers by itself to maintain the selected frame rate. The surfaces are stored as a single segment for which each pixel consists of two subsequent unsigned 8-bit integers. A line, in the X-axis, consists of 320 pixels. Within the surface exist 256 lines, all following each other. Figure 2.7 visualizes the data structure.

The pointer to the first pixel within the RAM is retrieved in the callback. The RTMaps output buffer is opened and the pixel information is copied into the output buffer by specifying the address of the first pixel and the size of memory to be copied, in case of a full frame of the Bobcat this amounts to 163840 bytes. After the surface is copied into the IplImage output buffer, the buffer is closed and available to be accessed by downstream processes. Subsequently, the callback thread is terminated. There can be more than one callback at the same time depending on the arrival rate of the surfaces in the RAM.

In the death section of the component, the MultiCam channel is deactivated, and then the driver is terminated. Note: The camera is responsible for the timing of all events downstream. The maximum operating frame rate of the camera is selected based on the performance of the DIP pipeline in terms of latency, further discussed in Section 3.1.4. In the case of the FPA developed in this thesis, this number was 72.5 FPS.

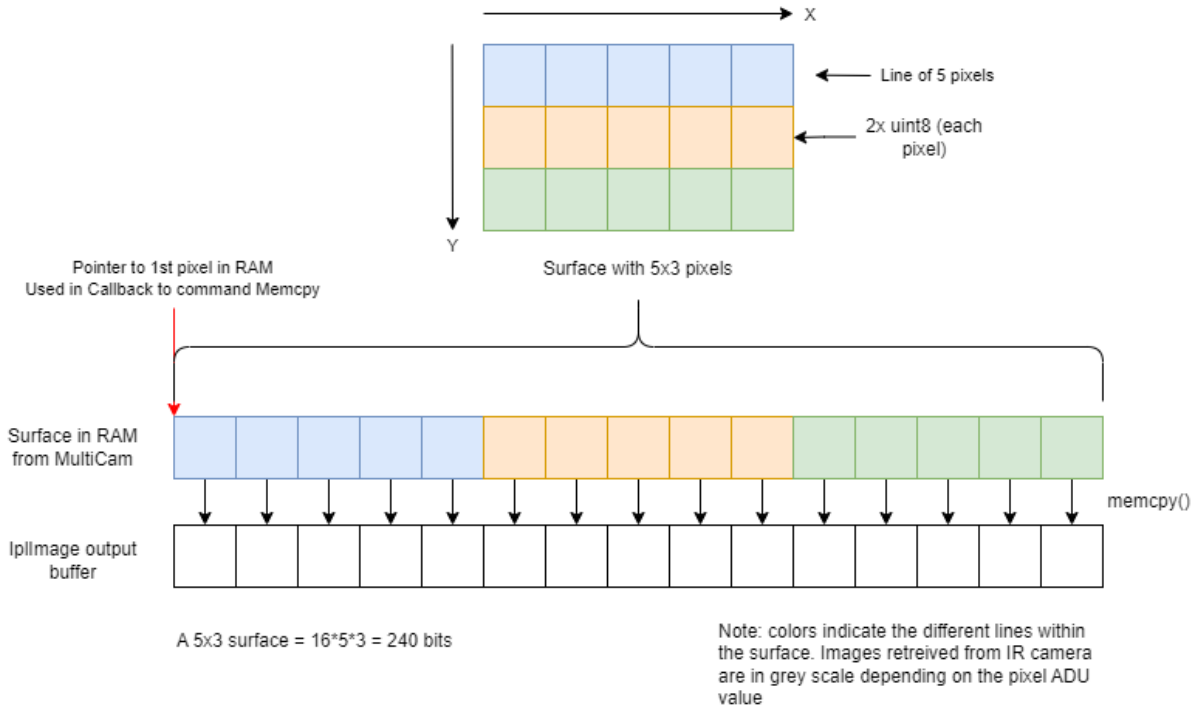

Figure 2.7: Data structure of full frame surface

COG component

The subsequent custom RTMaps component performs the tracking algorithm by finding the Center Of Gravity (COG), shown in Equation 2.1 and 2.3. The COG algorithm performs a weighted average with the received power per detector pixel (P_i) as the weight for its location (x_i or y_i). Here, i represents the index of a pixel.

$$x_{cog} = \frac{\Sigma_i P_i \cdot x_i}{\Sigma_i P_i} \quad \forall i = [0; 81919] \tag{2.1}$$

$$y_{cog} = \frac{\Sigma_i P_i \cdot y_i}{\Sigma_i P_i} \quad \forall i = [0; 81919] \tag{2.2}$$

The component iterates through all pixels within the surface inherited from the FIFO buffer. The data structure in memory is still a single sequence of pixel values. To note down the location of each pixel the index of each iteration is used to compute back the coordinate of the pixel onto the detector. This is done using Equation 2.3, 2.4. The half pixel is added to bundle all the power emitted onto the pixel in the middle of the pixel. Note that s represents the pixel pitch of $20\mu m$.

$$x_i = s((i\%320) + 0.5) \tag{2.3}$$

$$y_i = s(\lfloor i/320 \rfloor + 0.5) \tag{2.4}$$

Tests to verify the implementation of the COG algorithm showed that the optical power emitted onto the detector is quite low compared to the noise floor, as further discussed in Section 2.3.4, a threshold power level is imposed to prevent the COG from being influenced by the background noise. Without this threshold, the COG is not influenced by an angular deflection of the FSM. The threshold was sized based on the noise analysis in Section 2.3.3 and sets $P_i = 0$ if the analog-to-digital unit (ADU) level on that pixel is below the threshold. This way, pixels below the threshold do not influence the weighted average.

Convert component
After the COG is found for both axes, the pixel location is converted to angular displacement using Equation 2.5, applied to both X and Y axis respectively. Refer to Figure 2.8 for the various definitions. x_{mid} is the pixel location of the frame-centered coordinate system, s is the pixel pitch of the detector, and f represents the focal length of the focusing lens.

$$\Delta\theta_x = \arctan\left(\frac{(x_{COG} - x_{mid}) \cdot s}{f}\right) \tag{2.5}$$

Note, each time the FPA is started, the operator will have to check the x_{mid} and y_{mid} values in order to deal with misalignment in the optical setup. This does not influence the performance of the closed-loop FPA as this misalignment presents itself as a steady-state error, which will be controlled away. However, for data visualization and characterization purposes, re-calibration is needed.

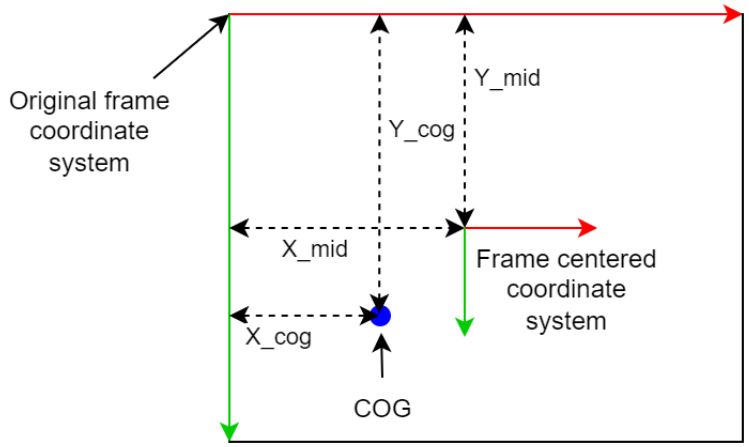

Figure 2.8: Definition of the various coordinate systems within the DIP toolchain.

2.2.3. Optical Design

The optical setup of the lab version of the FPA was built with a practical design philosophy. Optical elements were added in order of appearance to the incoming beam, starting with the laser source.

Customer requirement **FPA1-1A** dictates both a setup of FPA optical path and disturbance simulation. To this end, two FSMs in series were used. One to introduce disturbances in an undisturbed beam, the other to correct for these disturbances.
The laser source (LDM1550) used for this setup, as specified by Table 2.1, emits a collimated beam which, for this thesis, is assumed Gaussian. Even though the beam diameter is $3mm$, 2" bulk optics were used to mitigate problems with Numerical Aperture (NA) or spherical aberrations. A folding mirror reflects the light onto FSM-B (OIM5001). To prevent linear shifts in the projected beam onto FSM-A (OIM102), a beam expander of ratio 1 was made from two $100mm$ biconvex lenses $200mm$ apart. This introduces a new focal plane of which FSM-A takes an image. FSM-A projects the beam into the 50:50 beam splitter. In the future, the uninterrupted path will be projected by a focusing lens onto the SMF mode field. The folded path is imaged by a 100mm focusing lens onto the detector plane of the IR camera. The optical design can be consulted in Figure 2.9 and the used components are listed in Table 2.4, a complete list of components can be found in Table C.4.

Component	Part-number	Supplier	Quantity
Laser diode	LDM1550	Thorlabs	1
Neutral Density filters	NEK40A, NEK20A, NEK02A	Thorlabs	1
2” flat aluminum mirror	ME2-G01	Thorlabs	1
Bi-convex 100mm lens	LB1630	Thorlabs	3
Beam splitter 50:50	CCM1-BS015/M	Thorlabs	1
1” FSM	OIM5001	Optics In Motion	1
2” FSM	OIM102	Optics In Motion	1
Bobcat 320-CL	FC03	Xenics	1

Table 2.4: Components used in the optical setup of the FPA.

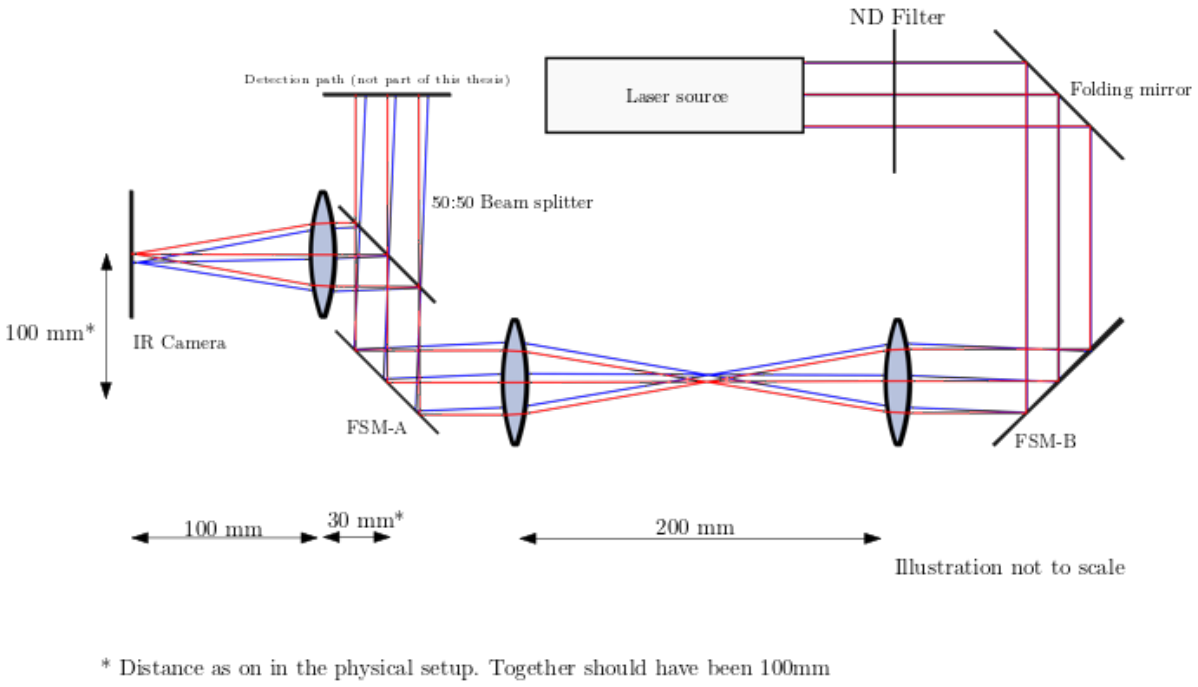

Figure 2.9: Ray tracing diagram to illustrate the optical setup of the FPA.

As seen in Figure 2.9, an angular motion of either FSM relates to a linear displacement of the beam projection onto the IR camera detector. The summed effect of both FSMs in terms of linear displacement can be transformed to the angular displacement of the optical axis by Equation 2.6, for which Δl is the linear displacement, f the focal length of the focusing lens, and $\Delta\theta$ the angular displacement.

$$\Delta\theta = \arctan\left(\frac{\Delta l}{f}\right) \tag{2.6}$$

NOTE: While performing verification, it was discovered that FSM-A is not in the focal plane of the focusing lens of the IR camera. The FSM is positioned $30mm$ in front of the focal point (further away from the lens). This was an oversight. The misplacement affects the accuracy of the beam location on the detector as the beam focuses before reaching the detector Figure 3.4. Though this mistake was found, the implications are limited as the discrepancy in beam location and the estimated location is small. This is further discussed in Section 3.1.3.

2.2.4. Control design

As a baseline FPA control design for MISO, two SISO parallel PID feedback controllers were envisioned. Each controller acts on a plant that behaves like a 2nd order LTI spring-damper-mass system. The control loop topology design is presented in Figure 2.10. This control topology featuring unity gain feedback was selected for its simplicity and the availability of loop shaping tuning methods [32, p.281].

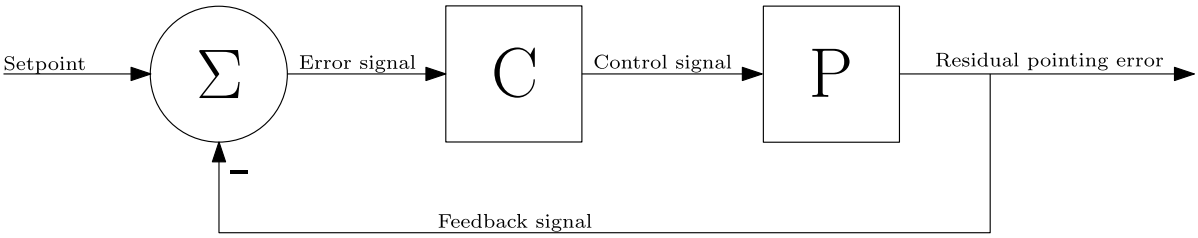

Figure 2.10: FPA feedback control topology for which C is the controller and P is the plant.

The bandwidth of the FPA in this thesis is limited by the sampling frequency of the IR camera. Open-loop (OL) SI, further discussed in Section 2.3.1, shows the frequency response limited by the observation frequency in Figure 2.11. The plant resides in the spring-line ($1/k$) regime of 2nd order mass-spring-damper system [32, p.282]. This line is centered around $0dB$ due to the presence of the OIM100 PID controller, contrary to what can be expected of 2nd order systems.
At this max sampling frequency of $72.5Hz$, the OL response shows Zero Order Hold (ZOH) behavior, as shown by comparison of the ZOH model and experimental data in Figure 2.11.

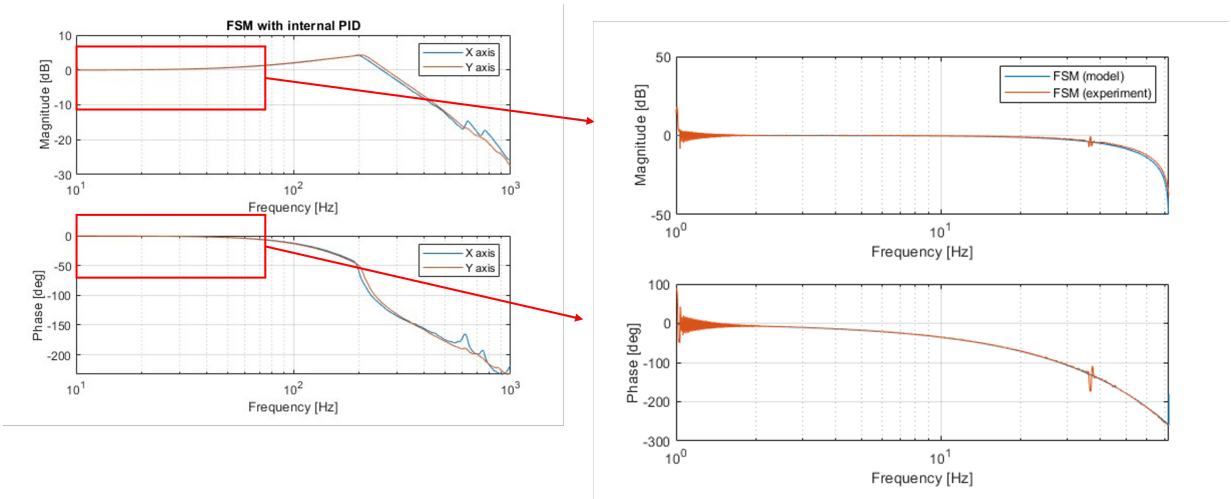

Figure 2.11: OL Bode plot of FSM-A measured with internal sensor (left). OL Bode plot of FSM-A measured with IR camera (right).

The tip-tilt PSD mentioned in Section 1.2 was introduced at the final stages of this thesis. For this reason, the control system was initially tuned to a flat uniform spectrum. The rationale was that a controller with low gain on frequencies higher than its bandwidth would work for any PSD for that frequency range. In hindsight with the tip-tilt PSD in mind this might not be the optimal design approach to minimize residual total disturbance energy, this will be further discussed in Section 4.2. An iteration in controller tuning was not performed due to time constraints.

As the dynamic responses of both axes of the plant are nearly identical, the controllers were tuned in the same way. Based on the OL frequency response, the controller was chosen to be an I-controller tuned using loop shaping [32, p.285], the controller selection is summarised in Table 2.5.

controller element	Desirable effect	Penalty	Implemented (Y/N)	Motivation
P	Increase all gain at zero phase cost	Sudden & steep cross over	N	Frequencies around Nyquist frequency also amplified.
I	Mitigate steady-state error & clear gain cross-over	-90 phase lag extra	Y	See desirable effects
D	Increase phase margin at cross-over & add damping	Taming required, increase in complexity	N	Damping already in the internal PID.

Table 2.5: Trade-off table for FPA controller topology.

A P-controller would be marginally stable because of sudden and steep crossover [32, p.283]. Although there is no penalty in phase for any P-gain, it also amplifies frequencies around the Nyquist frequency, which was considered undesirable. D-control was deemed unnecessary because the phase margin at I-controlled crossover is $> 30^{\circ}$, there is no need for extra phase lead.

I-control removes the steady-state error observed in earlier tests. Since there is no differentiator action (D-control), the frequency at which the I-Controller can be used can be higher. Given the flat OL ZOH behavior of the plant, which sits just below 0dB, and the OIM 100 control box with its internal PID, an I-controller is considered the most suitable control architecture. Bode-plots of the loop shaping method imposed on the analytical model are shown in Figure 2.12, displaying the plant, controller, and combined dynamic behavior.

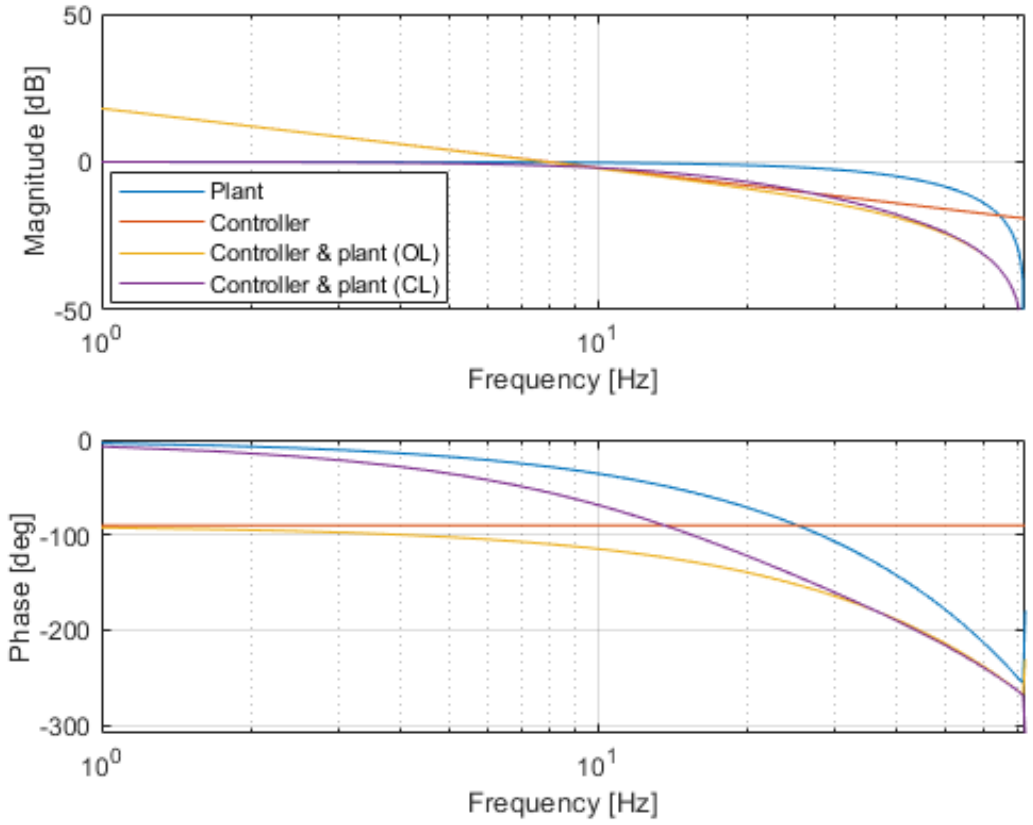

Figure 2.12: Bode plots of components of the FPA model demonstrating the loop shaping method.

The controller response was initially formulated in the continuous control domain [32, p. 282]. However, a discrete controller is needed because $f_{sample} < 1/10 \cdot f_{drive}$ [32, p.320]. Therefore, the controller is transformed to the discrete control domain using the Tustin transformation [32, p. 334]. The resulting control model Equation 2.7 leaves only K_i to be tuned.

$$C(z) = K_i \cdot \left[\left(\frac{T_s}{2} \right) \cdot \left(\frac{z+1}{z-1} \right) \right] \tag{2.7}$$

The OL analytical model is formulated by Equation 2.8. T_s represents the sample time [s]. T_l is the latency added to the ZOH [s]. An additional 0.003025s were observed in the SI data. The analytical model is compared against the experimental data in Figure 2.13.

$$T_{FPA_{OL}}(f) = \frac{K_i}{i2\pi f} \cdot \left(\frac{1 - e^{-i2\pi f T_s}}{i2\pi f T_s} + e^{i2\pi f T_l} \right) \tag{2.8}$$

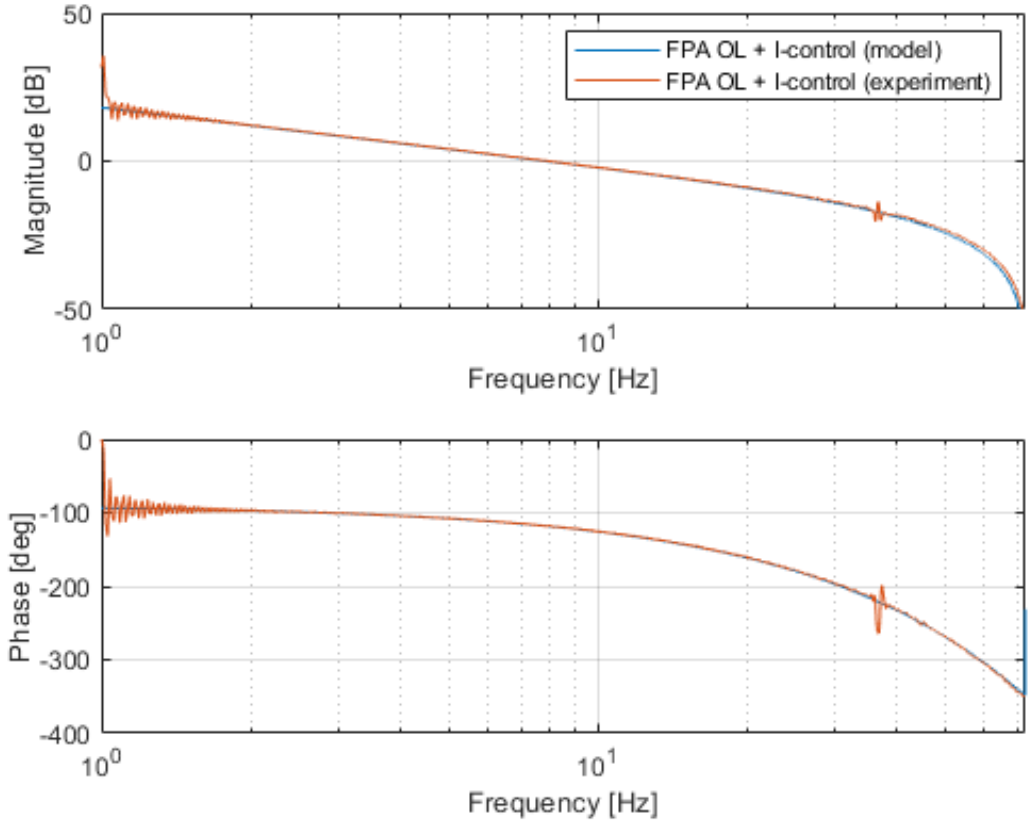

Figure 2.13: Open loop dynamic response of the FPA under I-control.

To obtain the closed-loop (CL) model Equation 2.9 was used.

$$T_{FPA_{CL}}(f) = \frac{T_{FPA_{OL}}(f)}{1 + T_{FPA_{OL}}(f)} \tag{2.9}$$

The controller is designed to cross 0dB on 8Hz because, in CL, there is no resonance peak after crossover, shown in Figure 2.13. The K_i gain of the I-Controller was selected to be $8Hz \cdot 2\pi = 50.2655$ [32, p.285]. The discrete model for the FPA control system is shown in Figure 2.14.

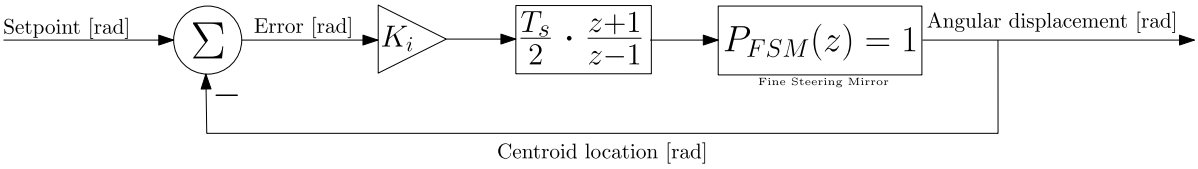

Figure 2.14: Discrete control system model running with $Ts = 1/72.5s$

The control systems described in Figure 2.14 are implemented in a Simulink environment, which, when compiled and uploaded to the MLBX, is monitored using ControlDesk.

Figure 2.15 shows the implementation of the control system, receiving the feedback signal over UDP and forwarding the command voltage signals to FSM-A. Within Simulink, the control signal is generated from the feedback and setpoint. Meanwhile, ControlDesk records ADCs for monitoring purposes. Lastly, the Simulink environment commands FSM-B to introduce the disturbance.

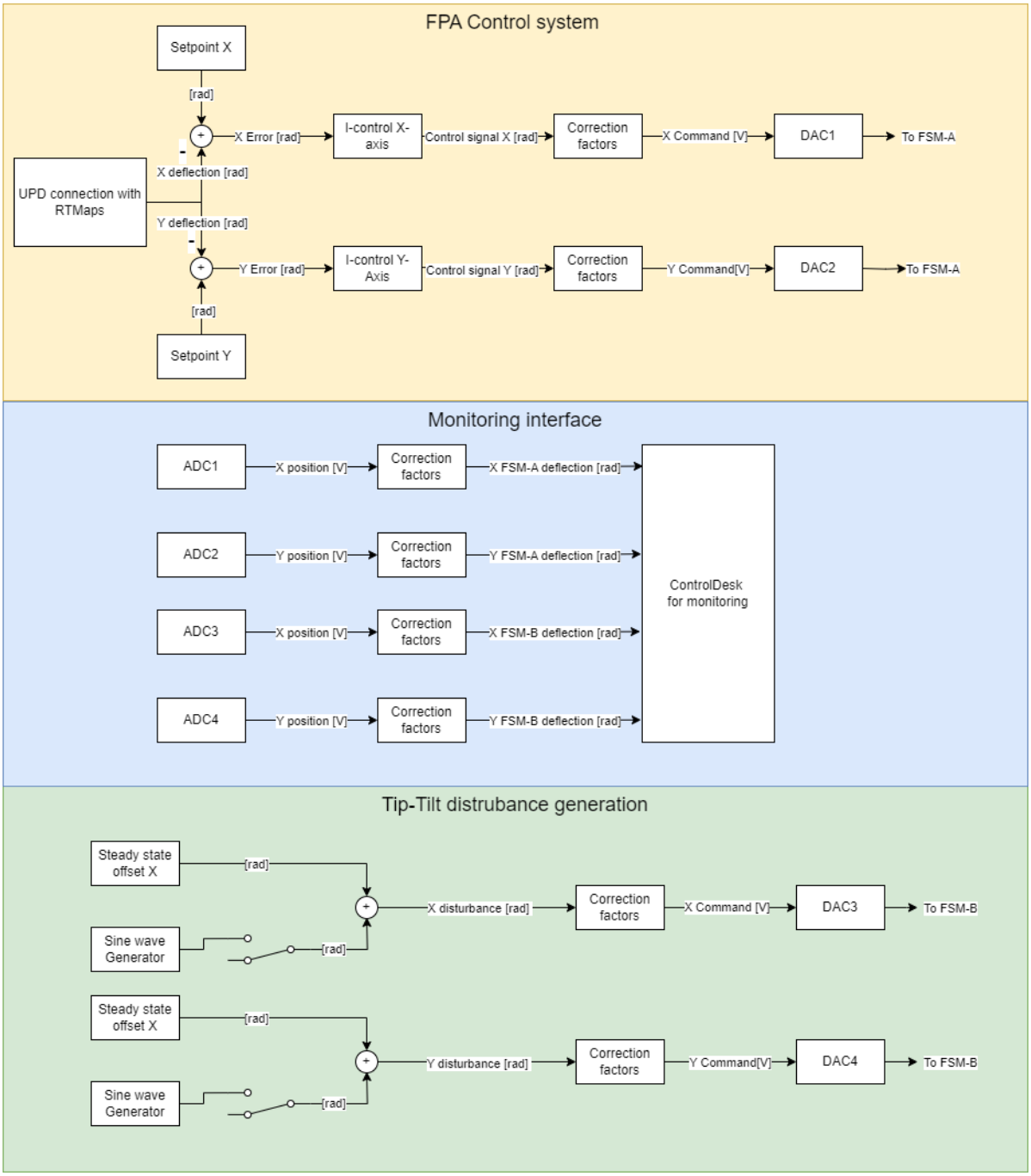

Figure 2.15: Implementation of FPA control system within Simulink environment

2.3.Performance characterization

This section introduces the methods used to characterize various important performance aspects related to the compliance of the FPA design with the system requirements.

2.3.1. Determine dynamic response using System Identification

Identifying the frequency response of the FSMs was done using a lock-in amplifier [40, slide 44-48]. The OL frequency response was measured using the setup in Figure 2.16. Driving one axis of either FSM-A or FSM-B with a sine sweep with $500\mu rad$ amplitude over $1Hz - 72.5Hz$. The return signal, mixed in the lock-in amplifier, was coming from the IR camera. The frequency response of the FPA is shown in Figure 2.13.

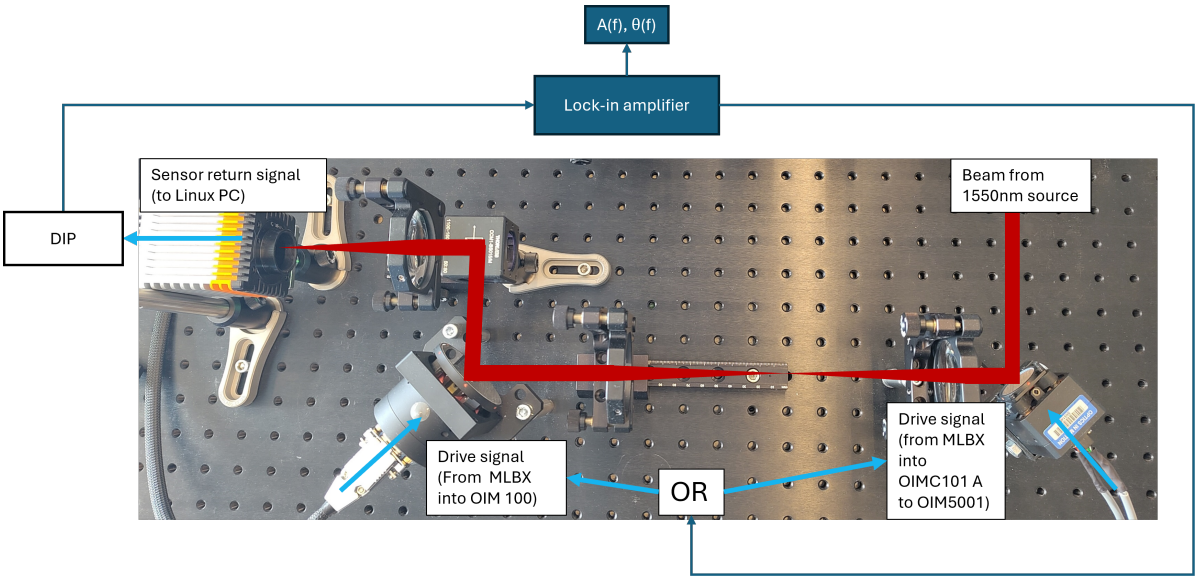

Figure 2.16: System Identification architecture of the open loop FPA.

The CL frequency response was measured using the setup in Figure 2.17. Driving one axis of FSM-B with a sine sweep with $500\mu rad$ amplitude over $1Hz - 72.5Hz$. The return signal, mixed in the lock-in amplifier, comes from the optical sensor in FSM-A, then multiplied by -1. A gain of $0dB$ indicates that FSM-A compensates FSM-B exactly. The frequency response of the FPA is shown in Figure 3.6.

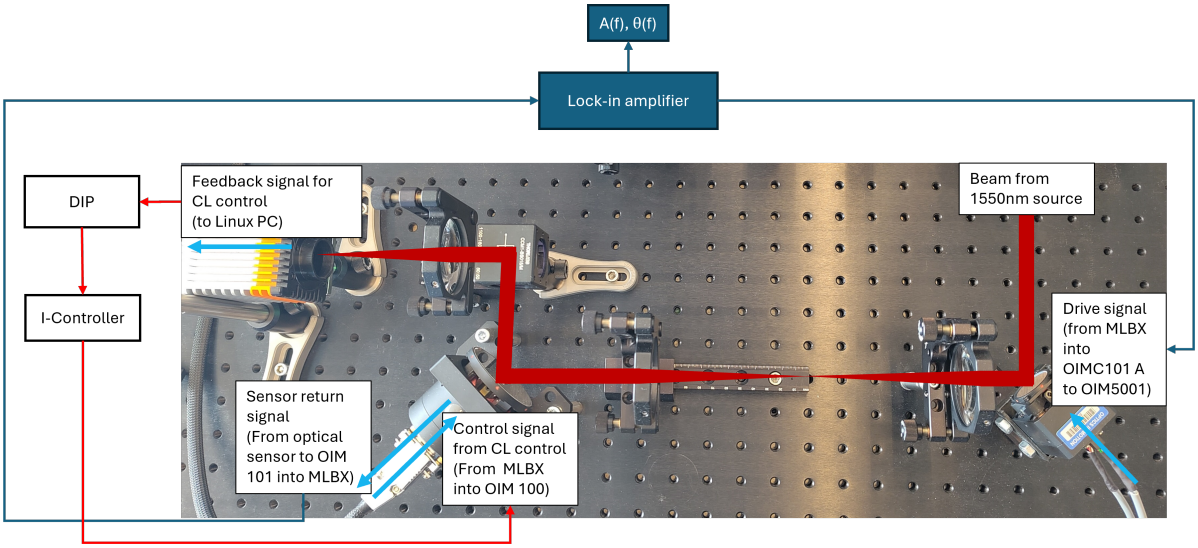

Figure 2.17: System Identification architecture of the closed loop FPA.

Using the lock-in amplifier in a system with a low sampling rate, some extra considerations were made based on observations during verification tests. The lock-in amplifier has a single ”sampling”/discretization frequency for both drive (Y_m) and sample signals (Y_{r1}&Y_{r2}). Discretization of the drive signal at higher frequencies causes the drive signal to become essentially a block wave instead of a smooth sine. This occurs approximately when the drive frequency is >1/3 of the sampling frequency or when less than five samples per period are made. This causes ZOH effects in the drive signal. Phase shifts can no longer be attributed to the plant only. It is difficult to apply the low-pass filter (LPF) under these conditions, and oscillations are visible in the output of the lock-in amplifier.

Oversampling of the drive and return signal was used as a solution. This solution solves the drive signal problem with the plant as a smooth sine executed. Figure 2.18 shows a block diagram of the various sampling times. A new potential problem is that the return signal is sampled in between its sampling points. ZOH1 effects of the return signal from the optical sensor are dominant in the recorded frequency response.

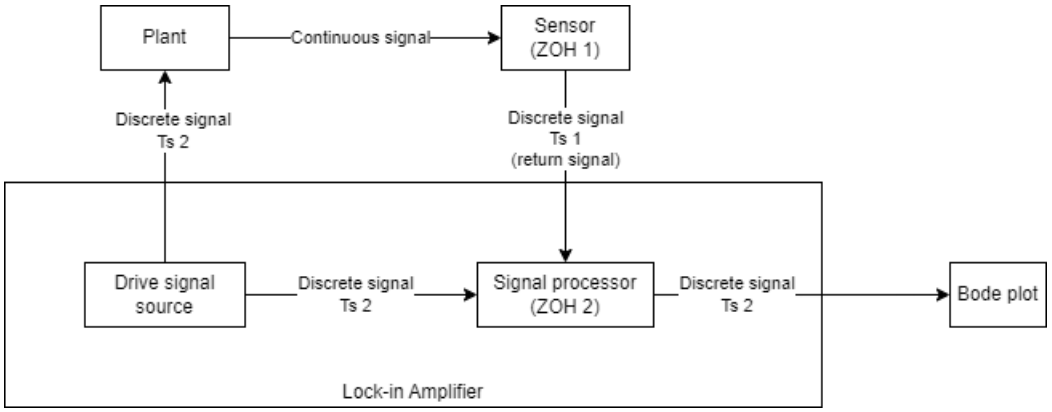

Figure 2.18: Block diagram of the testing architecture of the FPA, which is oversampled by the Lock-in amplifier.

Oversampling effects are visible when the differences in sampling intervals are small compared to each other. Extra latency is introduced due to oversampling by ZOH2, shown in Figure 2.18. The additional latency, and therefore, the phase shift, is at most 1 sample.

Next to the additional latency, oversampling also affects the resolution of the amplitude and phase estimations. In between intervals of the ZOH1, the amplitude and phase vary at the frequency of ZOH2, while the return signal properties remain constant at that interval. These variations degrade the accuracy of the amplitude and phase readings. Empirical spot checks revealed during verification that for all samples made by ZOH2 within the sampling time of ZOH1 the samples have a variation that limits itself to several decimal places behind the comma, an example of this is shown in Figure 2.19 for gain. The gain readings can be safely trusted up to 2 significant digits behind the decimal for the phase up to 3.

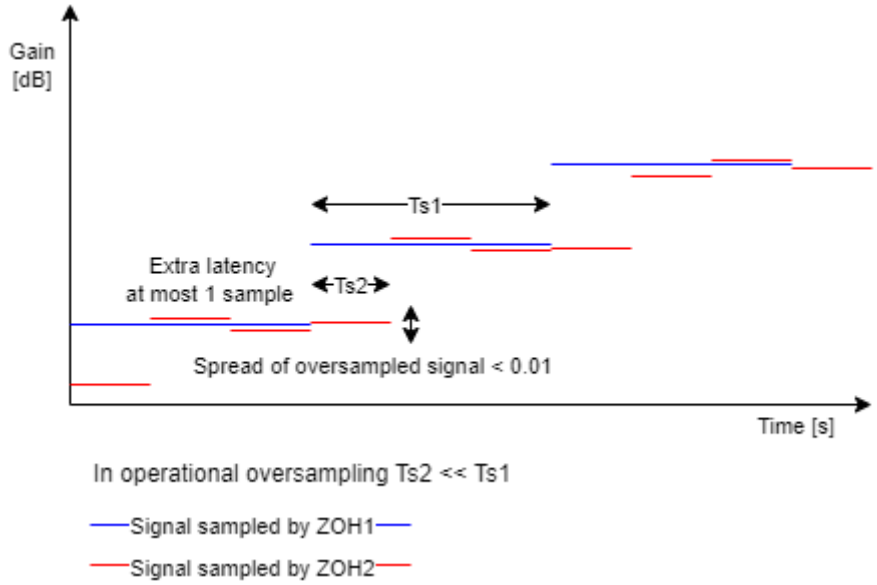

Figure 2.19: Representation of oversampling. Note: sampling intervals are not to scale.

Oversampling gives a close approximation of the frequency response, be it with less accuracy than would be achievable if the sampling frequencies matched, given that the oversampling is significantly faster. With this condition, additional latency, as a result of oversampling, becomes lower than the ZOH1 effects of the camera.

2.3.2. Measure Latency

Section 3.1.4 will discuss and quantify the latency effects on the FPA performance in more detail. However, a key conclusion is that the latency significantly impacts the FPA performance. Quantifying the latency and retrieving its origin is of importance. The FPA design in Section 2.1.3 is spread across various platforms. Therefore, different measurement strategies are used to set up a budget.

Verification tests indicated some stochastic properties are present in some of the elements in the FPA toolchain. The DIP implementation, for instance, has no direct authority in scheduling the OS resources required for the number of frames processed each second. A representative budget was obtained by recording latency for each component for $> 700,000$ frames. The law of large numbers (LLN)[41, p.185] was imposed to obtain an estimate of the expected latency and the respective variance.

Latency measurements were made in three segments: camera-frame grabber, RTMaps, and MLBX. The camera is commanded once upon start-up by the interaction with the frame grabber. Obtaining latency estimates within this interface is complicated as the interface can only be interacted with by the API of MultiCam. Euresys suggested using the timing method of RTMaps to estimate the latency of this system segment[2].

The above-described latency was estimated by subtracting RTMaps timestamps from successive frame arrivals. This time-between-frames (TBF) includes exposure, readout, transfer, and memory access. This latency estimate could not be broken down further within the time span of this thesis. The timestamp is generated immediately when the MultiCam driver triggers the callback function. Refer to Appendix B for a detailed sequence diagram of the DIP process. The timestamp thus indicates the moment in time that the frame is available as binary data within the RAM of the Linux platform.

RTMaps components were timed using timestamp propagation [42, p.198]. When a frame arrives within the RTMaps environment, a timestamp is generated. Each component, upon completion, records the time-of-issue (TOI), indicating how many μs have passed since the arrival of the frame. Individual component run times are then computed by subtracting the TOI values, this way the latency timing also

[2]Email conversation 18-03-2024

includes time spent in the FIFO buffers in between RTMaps component [43] as shown in Figure 2.20.

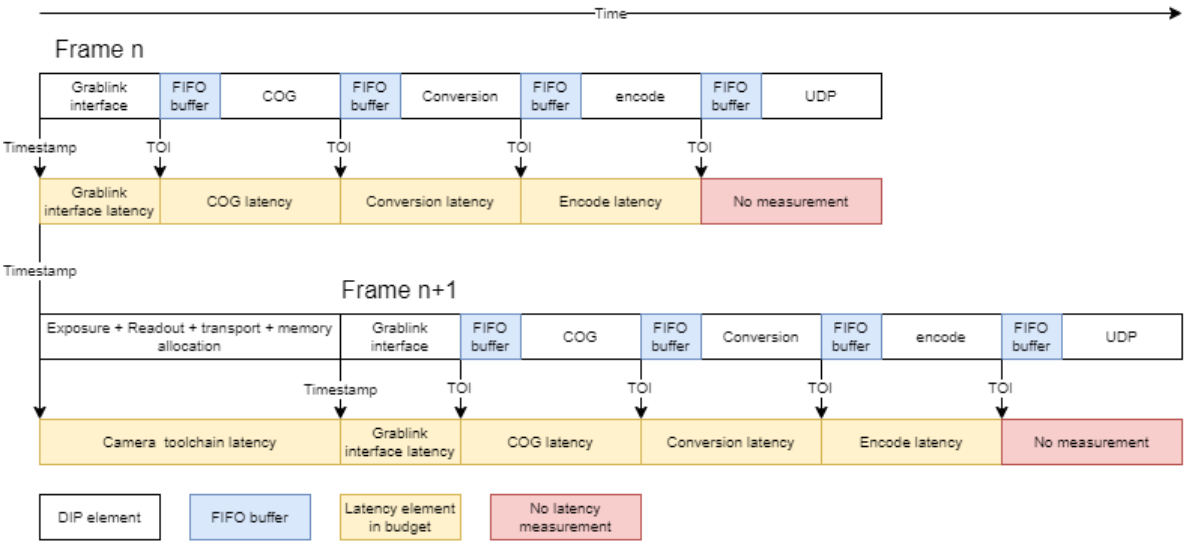

Figure 2.20: Latency measurement strategy in RTMaps. NOTE: elements are NOT to scale.

Latency measurements within the MLBX are difficult to obtain due to limited options in the user interface. The latency between input and output, for instance, in feedback control, is at most one time step. An explanation could be that this latency originates from the clocks not being synchronized between RTMaps and dSPACE. Therefore, the latency in the MLBX scales with the time settings of the Simulink model. In the Latency budget, a one-frame latency is accounted for, as observed in experimental data.

Timing the UDP interface has not been successful. The interface involves buffers and scheduling layers dictated by the Linux OS. As the total latency can be measured, the UDP latency is suspected to account for part of the discrepancies between the average budget and instantaneous measurement, as presented in Table 3.2.

2.3.3. Camera SNR budget

The pixel level signal-to-noise ratio (SNR) is an important metric for the FPA its tracking resolution, however also design of MISO. Within the greater context, the received optical power is split between tracking and data detection functionalities. The ability to operate the FPA at lower SNR leaves more power available for data detection and, thereby, more margin in the link budget.

The budget of a single pixel consists of the noise and signal sections. The budget is drafted in terms of electrons collected after each exposure.

Signal flux is considered always present, therefore the number of electrons collected is constant between different exposures. The electrons originating from the signal are computed by computing the optical power flux on the brightest pixel, obtained by experimental data or computed. This is then converted to photons using the photon energy, after which the signal is computed using Equation 2.10. Here P_{max} is the number of photons per pixel per second, t_i is the integration time and QE is the quantum efficiency of the detector.

$$S = P_{max} \cdot t_i \cdot QE \tag{2.10}$$

Noise is comprised of background noise and shot noise. The latter is the root mean square (RMS) value of the signal [44, slide: 42]. Background noise is a collection of all noises associated with the capacitive trans-impedance amplifier readout integrated circuit (CTIA ROIC) and is empirically obtained by taking a dark image at operational conditions, explained in Section 2.2.1. Background noise is stochastic and observed to be roughly normally distributed, as shown in Figure 2.22. For this reason, the RMS value is used in the SNR budget to account for the SNR variations between exposures. The dark image reveals

the noise distribution, $N(\mu_N, \sigma_N)$. The bias level, also used in the monte-carlo simulation (MCS), was removed from all data. The Noise RMS is found by Equation 2.11.

$$N_{RMS} = \sqrt{(\mu_N - Biaslevel)^2 + \sigma_N^2} \tag{2.11}$$

RMS values of both shot noise and background noise are added using Equation 2.12, similar to [44, slide: 50].

$$N_{tot} = \sqrt{N_{RMS}^2 + N_s^2} \tag{2.12}$$

The ADU levels are converted to electrons by dividing the full well capacity of the pixel by the number of ADU levels given the bits available, 14 in this case [45, Table 2-5].

With both average signal and noise electron quantities, the SNR is computed by division of the two. Note the dB conversion is as follows $SNR[dB] = 10 \cdot log_{10}(SNR[abs])$. Table 2.6 shows the SNR budget when $0.4\mu W$ is emitted onto the detector. Note that this budget can be applied to any pixel for which the ADU level is known. This will be used in the MCS presented later.

GENERAL PARAMETERS		
Parameter	quantity	unit
Emitted optical power	0.4	μW
Photon energy	1.28245E-19	J
Full well	125000	electrons
Bits/pixel	14	-
QE	0.8	-
Integration time	1.0	μs
Sensitivity of pixel	7.629	electrons/ADU
SIGNAL		
Parameter	quantity	unit
Expected flux (on brightest pixel)	6.03E+10	photons/s/pixel
Signal	48278.809	electrons
NOISE		
Parameter	quantity	unit
Expectation of noise (μ_N)	10100	ADU
STD σ_N	60	ADU
Biaslevel	9920	ADU
RMS shot noise	28.800	ADU
RMS Background noise	189.737	ADU
RMS shot noise	219.724	electrons
RMS background noise	1447.576	electrons
total RMS noise (N_{RMS})	1464.157	electrons
SNR		
SNR	32.974	-
	15.182	dB
Required SNR for COG	13.00	dB
Margin	2.182	dB

Table 2.6: SNR budget for brightest pixel on IR camera with 0.4 μW of emitted optical power.

2.3.4. Tracking resolution using Monte-Carlo Simulation

Beam tracking using the COG algorithm finds a pixel location on the detector based on the weighted average of the detected optical power. Before this number can be used to control the FPA with feedback, a metric is desired to quantify how well the actual beam position is tracked, expressed in detector resolution. This resolution represents the minimum observable change in beam position at a specific SNR.

For this thesis, a Monte-Carlo simulation (MCS) is used to quantify how many decimal places of the pixel location can reliably be used. By using an MCS, the LLN [41, P.185] ensures the estimated tracking accuracy converges to the actual performance.

Generating a model from experimental data containing detector bias and noise, the MCS finds the detector resolution without the need for a long calibration campaign or preprocessing. This last one is of importance as preprocessing frames on a pixel-by-pixel basis introduces extra latency.

For the MCS, the 2D COG tracking problem was simplified to a single 1D problem, applicable to both of the independent axes of FPA. The beam model was obtained by fitting the Gaussian profile to a 1D cross-section of the image with a laser projected onto it. An example of the fit is depicted in Figure 2.21.

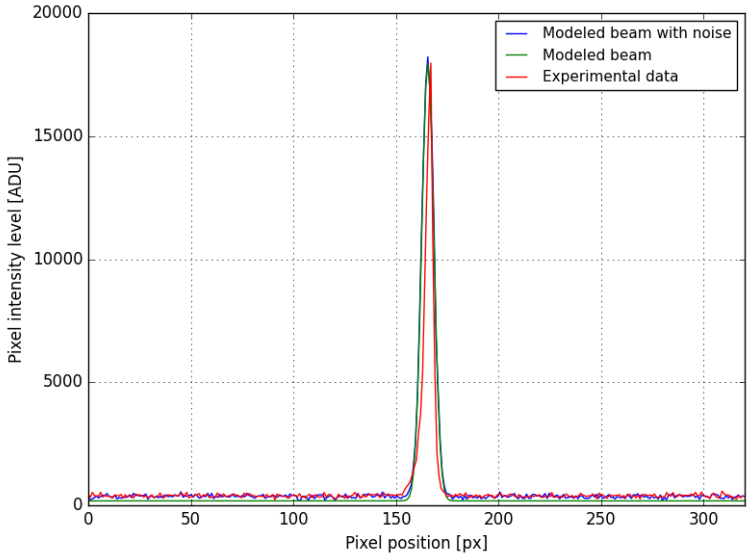

Figure 2.21: Beam model in simulation compared to experimental data at $0.5\mu W$ emitted power onto the detector (bias level removed).

The experimental data was generated with $1\mu s$ exposure and $0.5\mu W$ emitted optical power onto the detector, note that this power level is only used for verification of the model. The beam model is based on the shape of the experimental data within the units of the detected data. By default, it is a discretized version of a Gaussian beam model at a fixed distance from the beam waist, leaving only the radial component. The model represents the intensity profile as ADU due to the local integration and digitization of each pixel per exposure. The resulting beam model is presented by Equation 2.13.

$$P_m(x) = (P_{D_{max}} - 3\sigma_N) \cdot \exp\left(-2 \cdot \frac{(x - x_{cog})^2}{\omega} \right) + 3\sigma_N \tag{2.13}$$

$P_m(x)$ is the local power on pixel x. $P_{D_{max}}$ is the power level of the max illuminated pixel. σ_N obtained along with μ_N by finding the average and spread of all pixels in a dark image under operational conditions. Each pixel is assumed to independently draw its value from an identical distribution $N(\mu_N, \sigma_N^2)$ for this dark image. This distribution represents the noise before bias removal. Figure 2.22 shows the definition of the various levels along with the background noise distribution.

The additional $3\sigma_N$ in Equation 2.13 accounts for the bias level in the model. The local beam radius ω was found by fitting the model onto the experimental data and relates to the spread of the beam

projection. Testing confirmed that this spread measure remains the same for variations in emitted optical power levels.

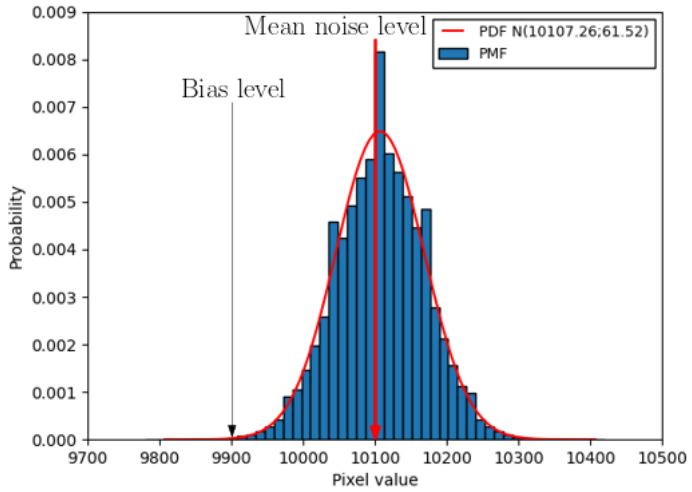

Figure 2.22: Noise distribution over a measured dark image under operational conditions.

x_{cog} is the pixel location of the simulated beam onto the 1D detector, and it will drawn in every instance of the COG simulation. This random variable has distribution $U(40, 280)$ to prevent clipped beam profiles due to detector edges.

To simulate noise, for each pixel on the 1D detector, a noise value from the noise distribution is drawn, consisting of normally distributed $N(3\sigma_N, \sigma_N^2)$ background noise with bias level removed, identified by analyzing the dark image under operational conditions. Additionally, the local shot noise is added. Local shot noise is assumed to approach a normal distribution with a standard deviation of the signal level. Since the expectation is 0 and no subzero levels can be attained, the absolute value is taken. The influence of the shot noise is limited. However, it does ensure the SNR definition is consistent for all analyses in this thesis.

The noises are added to the beam model, as described by Equation 2.14. Noises are considered independent sequences[46, slide 17]. Additionally, it is assumed that the pixel location variance is negligible.

$$P_e(x) = P_m(x) + N(3\sigma_N, \sigma_N^2) + \left|N(0, P_m(x)^2)\right| \tag{2.14}$$

The simulated beam with noise is then used to determine the COG using the same algorithm as implemented in the RTMaps component, explained in Section 2.2.2. Thresholding used. Pixels with levels below the threshold are set to 0. Using Equation 2.1, the COG algorithm computes an estimate of the beam center. The estimation offset is defined as the absolute distance between the generated COG and the estimated one. Shown by Equation 2.15.

$$x_{offset} = \left|x_{cog} - \widehat{x_{cog}}\right| \tag{2.15}$$

The model inputs are all Independent Identically Distributed (iid) sequences of random variables, so x_{offset} is also an iid sequence through propagation of independence [41, p.126]. The performance metric of the COG algorithm is obtained by repeating the above process n times such that the variance, Equation 2.17, around the mean of the estimator,Equation 2.16, reduces.

$$\overline{x_{offset}} = \frac{\Sigma_j^n x_{offset}(j)}{n} \tag{2.16}$$

$$s.e. = \frac{\sigma}{\sqrt{n}} = \frac{\sqrt{\frac{1}{n-1}\Sigma_l^n (x_{offset}(l) - \overline{x_{offset}})^2}}{\sqrt{n}} \tag{2.17}$$

The estimator $\bar{x_{offset}}$ is therefore found by the expectation of n independent variables x_{offset} along with standard error $s.e.$. The tracking resolution is based on the estimation offset along with its corresponding standard error. The estimation offset (+3 s.e.) with 97% confidence in the tracking resolution is computed using Equation 2.18.

$$\Delta\theta = \arctan\left(\frac{(\overline{x_{offset}} + 3 \cdot s.e.) \cdot s}{f}\right) \tag{2.18}$$

The simulation parameters can be found in Table 2.7. The simulation plan is presented in Figure 2.23.

Input	Meaning	Value	Unit
$P_{D_{max}}$	Level of max illuminated pixel	Varies per simulation campaign	[-]
μ_N	Mean background noise level	10100	[ADU]
σ_N	Variance of background noise	60	[ADU]
$\mu_N - 3\sigma_N$	Bias level	9920	[ADU]
ω	Beam radius at detector plane	35	[px]
n	Number of runs with the same power level	10000	[-]
s	Pixel pitch	20	[μm]
f	Focal length of focusing lens	100	[mm]
$T_{threshold}$	COG threshold value	650	[ADU]

Table 2.7: Simulation parameters for MCS estimating tracking resolution.

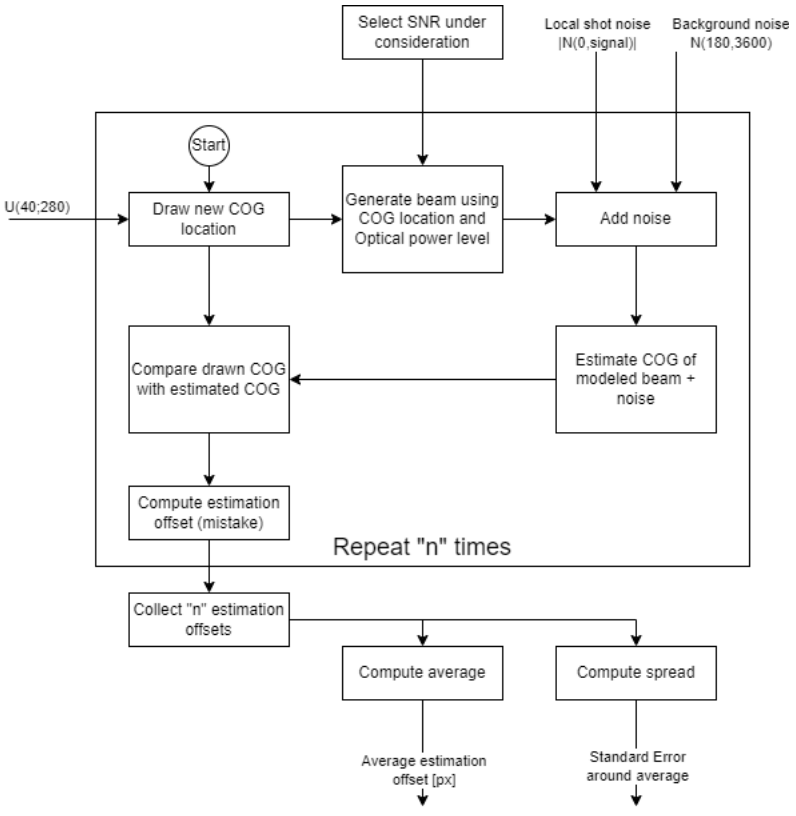

Figure 2.23: Simulation plan for COG estimation resolution characterization.

The simulation with n simulations of the same beam was performed on multiple levels of $P_{D_{max}}$ to estimate the COG performance on different SNR levels Figure 3.3.

3
Results & Discussion

With the Fine Pointing Assembly for MISO designed and developed, what remains is to understand and quantify its performance. This chapter presents performance parameters and dynamic behavior and verifies assumptions made in the design. Lastly, the limitations of the Fine Pointing Assembly are discussed.

3.1.Results

The results are divided among the domains presented in Chapter 2, starting first with the overall design followed by more in-depth results related to resolution, latency, and dynamic behavior.

3.1.1. Design implementation

Throughout the FPA development process, the system gradually increased in size and functionality. The system grew in accordance with the progression of the methodology as presented in Chapter 2, starting at the commissioning phase. After commissioning and interfacing, the SI campaigns were performed, followed by the camera characterization campaign. Finally, the control system was tuned and implemented. The final setup is presented in Figure 3.1. Several system characteristics of the FPA as a control system are presented in Table 3.1.

System property	Value	Unit
Sensing resolution*	20	μrad
Angular range	+/-0.02	rad
Total emitted optical power	0.8	μW
Tracking SNR margin*	2.2	dB
Bandwidth	8	Hz
Phase margin (OL)	56	$^{\circ}$
Gain margin	N.A.	dB
Effective tracking frame rate	72.5	FPS
Average latency	0.02069	s

Table 3.1: Table of specifications of FPA x-axis, y-axis has similar performance parameters. *After threshold correction to 650 ADU.

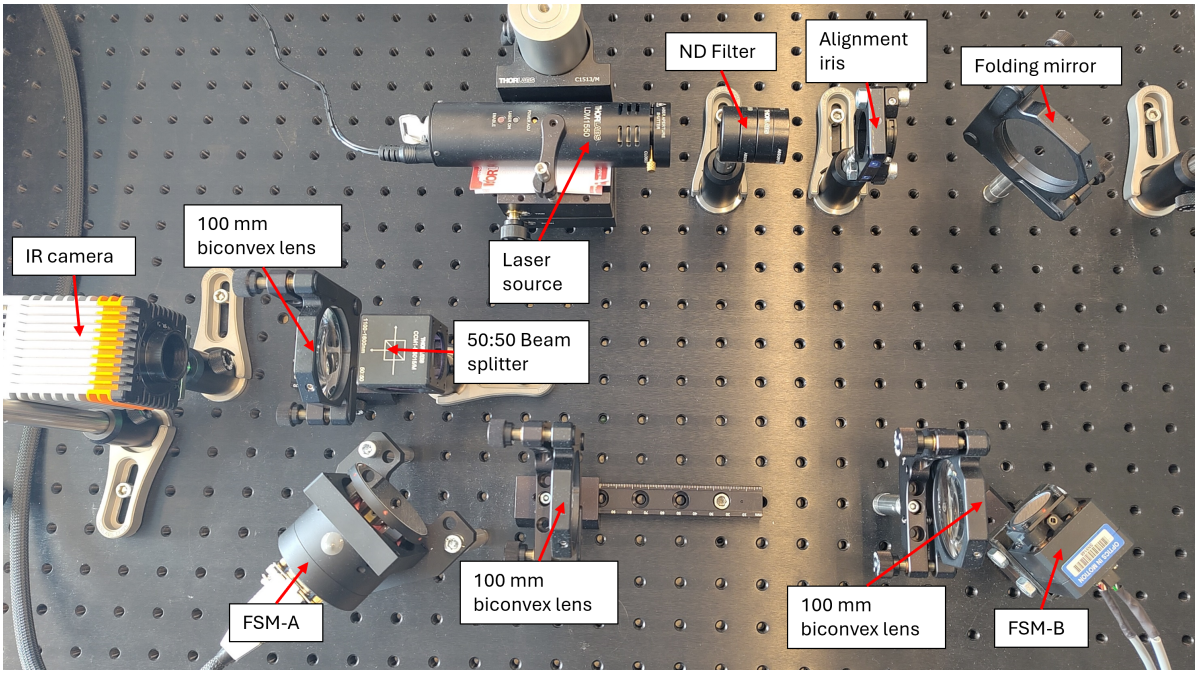

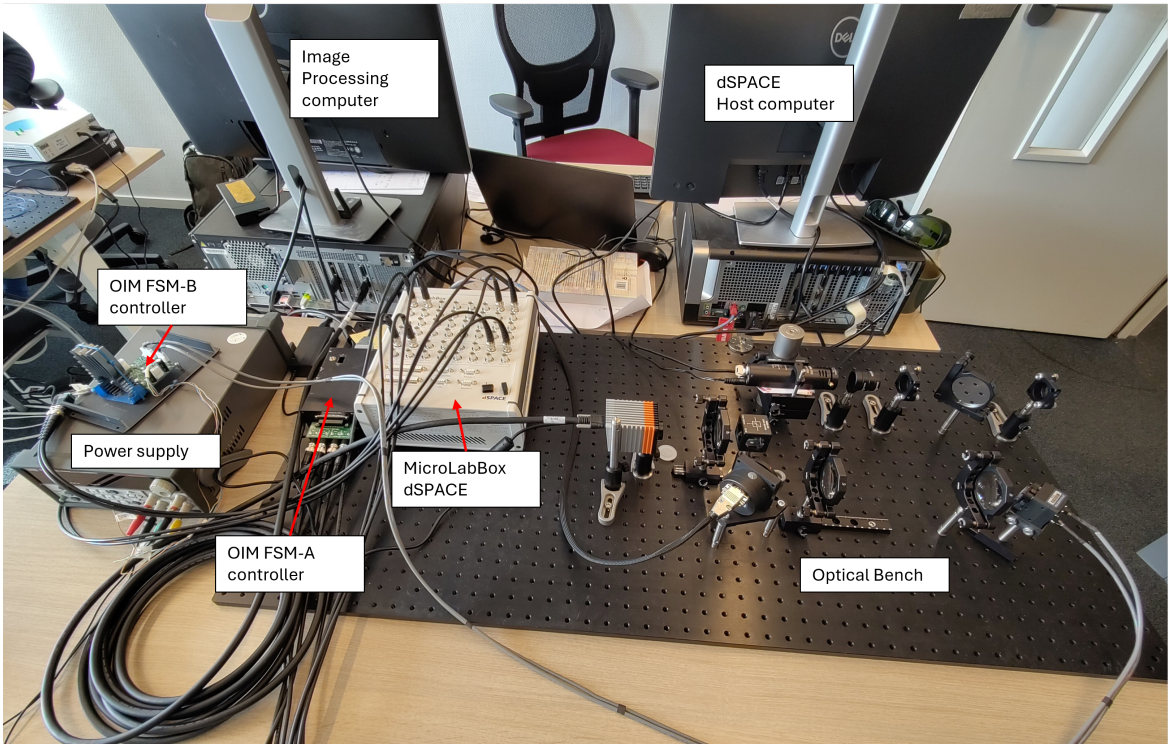

Figure 3.1: (Top) Optical bench of FPA, (Bottom) Full lab setup of FPA.

3.1.2. SISO assumption

The design and implementation of the FPA are based on the assumption that the tip-tilt disturbances in the beam can be removed independently. Since the Zernike polynomial expansion is a linear sum, the principle of superposition was exploited. To verify if this assumption was justified, the FSMs were tested to have two uncoupled axes of mirror actuation. The results for FSM-A are shown in Figure 3.2. Note that the first letter in the labels refers to the driven axis and the second to the monitored axis. These results were obtained using the OL configuration for SI.

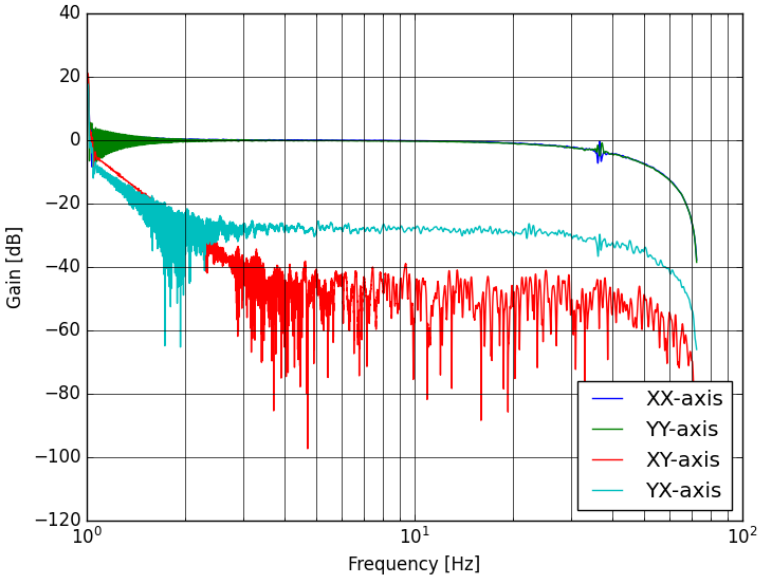

Figure 3.2: Frequency response OIM 102 FSM axes observed by IR camera.

The above figure shows that the X and Y axes have similar dynamic responses. This is also reflected when comparing the phase response in Appendix A. Additionally, the cross-coupling between the X and Y axes is -25dB or more throughout the whole relevant spectrum. Given these observations, it is considered justified to regard the FPA axes as two uncoupled SISO LTI systems. This justification is corroborated by a study of a similar FSM model (OIM 101) [47].

The IR camera readout and the tracking algorithm also support uncoupled readouts of both X and Y coordinates due to the use of a local Cartesian coordinate system, as demonstrated during testing.

All hardware and software elements in FPA have two uncoupled axes. For this reason, two completely isolated feedback loops were made. The assumption to design the FPA as two parallel SISO LTI control systems is thus considered valid.

3.1.3. Tracking resolution & acceptance range

As introduced in Section 2.3.4, the tracking resolution is closely related to the SNR of the IR camera. To identify the behavior of the tracking resolution under different SNR values, the MCS was run with the simulation parameters in Table 2.7. The results of the MCS are presented in Figure 3.3.

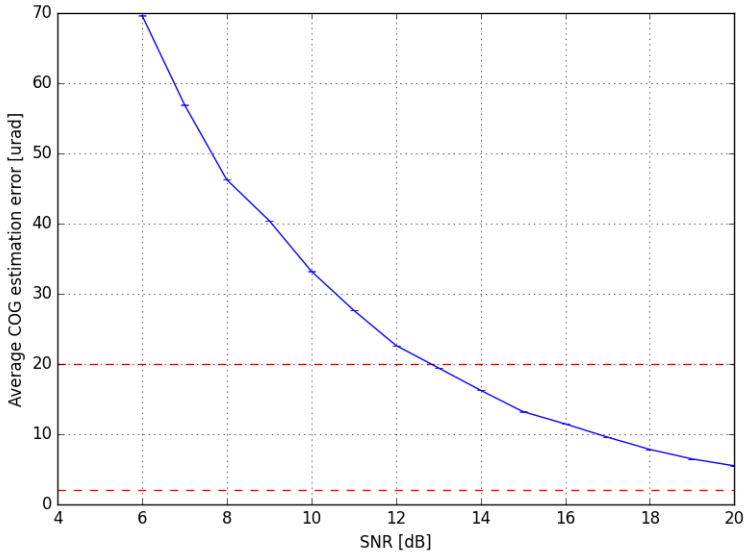

Figure 3.3: Simulated camera resolution at various SNR values.

The simulation indicates that SNR above $13dB$ can confidently use pixel resolutions up to 0.1 px, which with the current optical setup translates to $20\mu rad$ resolution. The resolution of 0.1 px is similar to what is used in OCLT [48, fig.8]. The operational FPA design has an SNR of $15.18dB$, therefore a margin of $2.18dB$. With a pixel pitch of $20\mu m$, a minimum throw of $2\mu m$, and a focal length of the focusing lens of $100mm$, using Equation 2.18 yields a tracking resolution of $20\mu rad$. These results show that **FPA1-3-2** is not met.

Additionally, during a verification campaign, an error was discovered in the MCS regarding the background noise model. After correction, the mean noise level was increased by $3\sigma_N$ compared to the original model. Therefore, some of the noise is shifted above the original threshold. The noise sometimes influenced the COG estimation and increased the estimation offset. The error is corrected in all analyses related to the SNR in this thesis. However, all SI runs were made with a too optimistic resolution, when in fact the resolution was $\approx 1mrad$, see Appendix A. Due to time constraints, the SI runs were not repeated. The delivered FPA does have a 0.1-pixel resolution as the threshold value is corrected for, hence the $20\mu rad$ resolution in Table 3.1.

As already briefly mentioned in Section 2.2.3, during the verification campaign, it was discovered that the focusing lens in front of the IR camera is not positioned correctly. Ideally, this lens would have FSM-A on its focal plane on one side while having the detector on the other focal plane. This is however not the case, the focusing lens has distance 100mm to the detector, however, 130mm to the FSM.

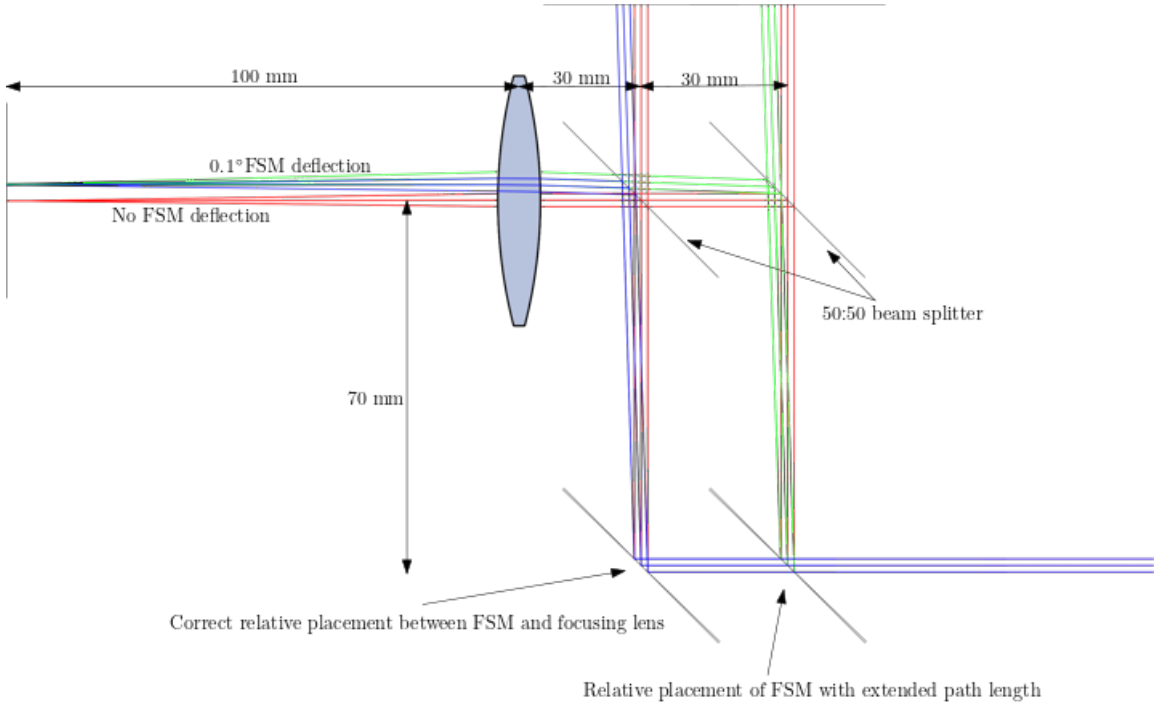

Figure 3.4: Ray tracing of the misplaced optical setup projected on top of the designed optical setup.

Figure 3.4 shows the two scenarios overlapped. Ray tracing shows that although the lens placement is off, the rays still roughly project the beam center onto the detector in the same place, be it both slightly out of focus due to the field curvature and extended path length in the case of the misplaced lens. Defocus is only affecting the tracking resolution if it is asymmetric, which for field angles $< 500\mu rad$ was not observed in the tests. This indicates that in both scenarios, the detector plane is likely within the depth of focus, and in this case, it is governed by the beam waist of the Gaussian beam. Therefore, the misplacement does not significantly influence the tracking resolution. Due to time limitations, the effect of the misplacement was not studied further.

The errors mentioned above will not affect the conclusions presented in Chapter 4 because the resolution does not influence the operational bandwidth of the FPA, it marginally influences the disturbance energy performance metric, does not influence the angular acceptance range of, the FPA, and is not related to latency. The error is contained within requirements **FPA1-3-2** and only indirectly **FPA1-3-1B**. The mitigation effort of changing the threshold corrects for **FPA1-3-2** as the misplacement of the focusing lens has an insignificant effect on the resolution. For **FPA1-3-1B** the impact is limited as the requirement is qualitative of nature. Even with the lower resolution, a significant reduction in disturbance energy is observable in the tip-tilt PSD.

The angular acceptance range of the FPA is limited by the maximum observable deflection of the FSM by the IR camera. In the commissioning phase of the FSM it experimentally was discovered that deflections in optical axis up till $\pm 0.02rad$ were observable in the full-frame, thereby satisfying **FPA1-3-3**.

3.1.4. Latency

Latency measurements were performed on the FPA as described in Section 2.3.2 and are presented in Table 3.2.

Source	Average latency [μs]	std [μs]	lower bound latency [μs]	upper bound latency [μs]
Camera	13820	320	12860	14780
RTMaps (all components)	194.367		28.696	386.694
Grablink interface	18.898	7.276	0.000	40.725
cog	144.064	38.456	28.696	259.432
conversion	17.145	9.044	0.000	44.278
encode	14.261	9.333	0.000	42.260
UDP socket (send)	No measurement	No measurement	No measurement	No measurement
MLBX-SL model (ZOH)	6896.552	0.000	6896.552	6896.552
total	20910.919		19785.248	22063.246
Measured	20689.655			

Table 3.2: Latency budget in FPA control system running at 72.5Hz.

Even though the initial frame rate of the DIP toolchain was intended to be 400 FPS, the TBF measured during verification indicated that the effective maximum frame rate of the FPA is 72.5 FPS. This can be seen in Figure 3.5 in which the MLBX samples at $145Hz$. The figure shows that the RTMaps signal (blue line) only changes once every two samples, effectively providing feedback only at a rate of $72.5Hz$.

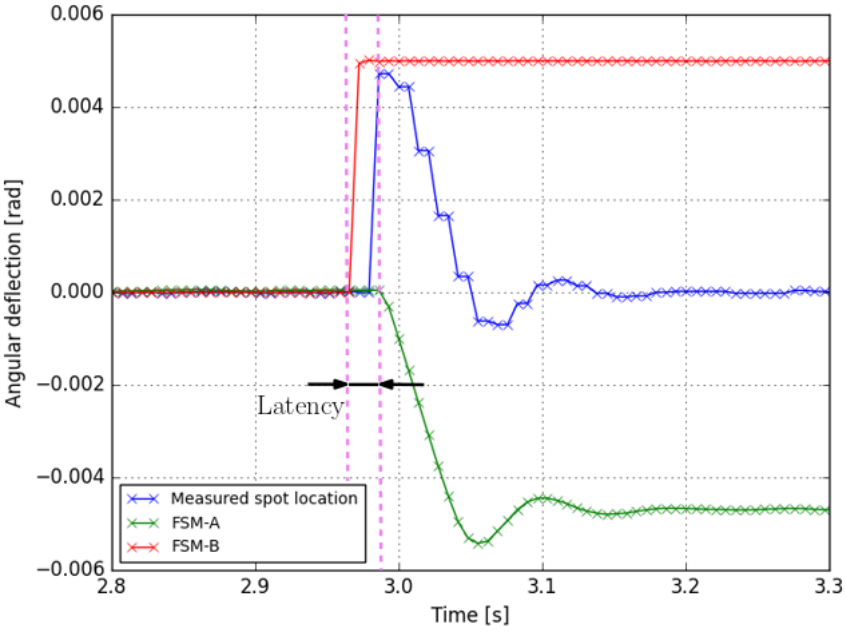

Figure 3.5: Step response of the X-axis sampled by the MicroLabBox at $145Hz$.

The budget, in Table 3.2, shows that the majority of the latency is found in the software on the processing computer. Specifically, the resource allocation in the image processing computer is when interfacing between frame-grabber and RTMaps. At lower FPS settings, the latency of the above process increases. This behavior is counterintuitive and is speculated to relate to the OS assigning fewer resources.

Conversations with Euresys revealed there was a mismatch in the frame grabber setting. Correcting the mismatch increased the effective FPS to roughly 100. Therefore, the mismatch is not considered the root cause of the observed latency and was not implemented as the performance would only marginally improve. The settings mismatch was not further implemented due to time limitations. Sampling at higher frequencies leads to better frequency response estimations at higher frequencies. So, the controller can be tuned to get a higher bandwidth, however, similar problems related to latency will arise at this elevated bandwidth.

The measured total latency presented in the budget was verified by measuring latency in a step response through the dSPACE interface, presented in Figure 3.5 by the pink dashed lines. The sampling setting of dSPACE limits latency measurements with higher resolution.

Latency dominates the phase performance of the FPA operated at lower frequencies and is on average $2.07ms$. The biggest contribution of latency can be found in the grablink-RTMaps interface, accounting for roughly 67% of the total latency. Because the latency associated with DIP is causing the loop frequency, and therefore bandwidth, to be lower than desired the requirement **FPA1-1B** is considered not yet met as it automatically implies the non-compliance of requirement **FPA1-3-1A**.

3.1.5. Dynamic behavior

The dynamic response of the CL FPA is presented in Figure 3.6. The achieved OL gain crossover bandwidth is 8Hz. The bandwidth requirement **FPA1-3-1A**, thus, is not met. Again, the X and Y axes have a nearly identical dynamic response. Therefore, only the X-axis is shown.

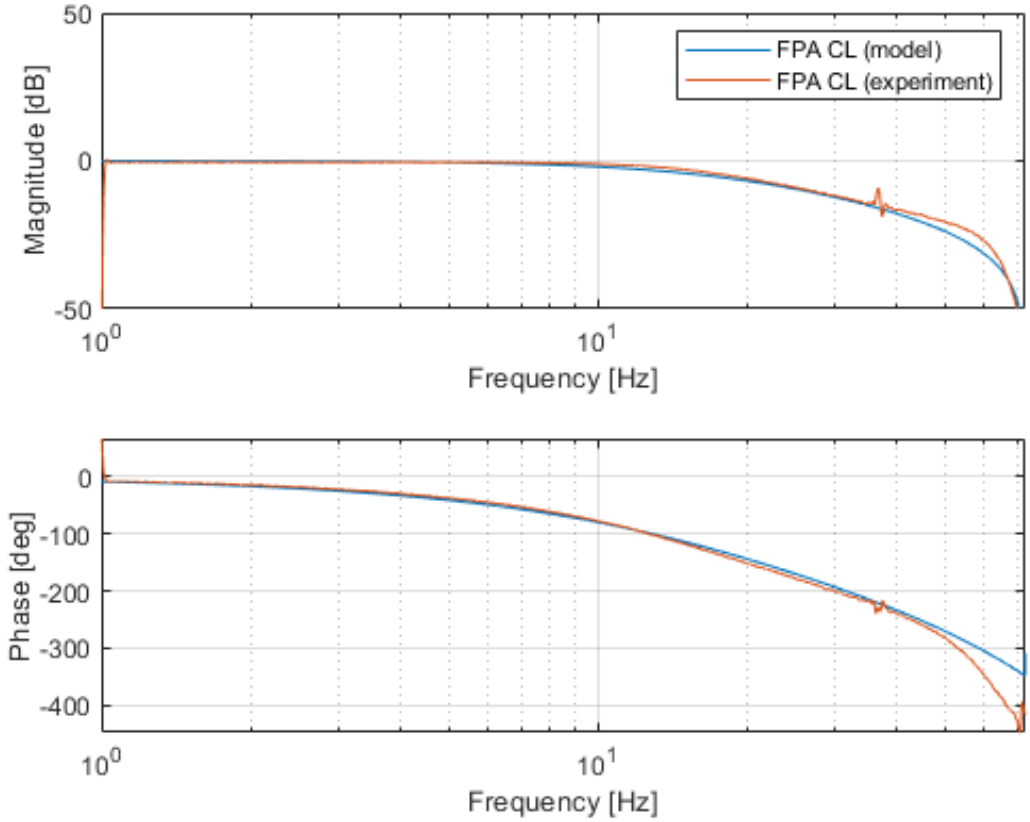

Figure 3.6: Dynamic response of closed loop FPA for both model and experiment.

System requirement **FPA1-3-1B** dictates the assessment of the FPA performance as a high-pass filter for tip-tilt disturbances. The FPA performance is measured by comparing the total disturbance energy of propagated tip-tilt single-sided PSD through the dynamic response of the FPA against its original value.

The tip-tilt spectrum is obtained through Equation 1.2, and 1.3, introduced in Section 1.2. The propagation of the PSD through the FPA is achieved through Equation 3.1 [49, eq:19]. Note that this expression is altered to reflect the transmittance of energy through the FPA. In this formulation, the energy within the new PSD reflects the energy that was not removed by the FPA.

$$PSD_{new}(f) = (1 - |T_{FPA}(f)|^2) \cdot PSD_{Glindemann}(f) \tag{3.1}$$

$T_{FPA}(f)$ is the transfer function of the closed loop system. The above equation indicates that only the magnitude is relevant to this propagation. Both analytical and experimental CL dynamic behavior were propagated. However, these were first assessed side-by-side in Figure 3.6. Though the match is not perfect, it is considered sufficient up to 36Hz, the Nyquist frequency. Discrepancies beyond this frequency could be related to the dynamic response of the FSM itself, however, due to the limited sampling frequency and the effect of the ZOH this is not certain. The discrepancy is most severe for phase, which is not considered for propagation of the single-sided PSD. Later, it will become clear that discrepancy does not cause significant differences in remaining disturbance energy. In the interest of time, the origin of this discrepancy is not explored further.

Subsequently, both the analytical and experimental FPA propagated the original PSD to generate the altered PSDs, revealing the FPA performance as a high-pass filter Figure 3.7.

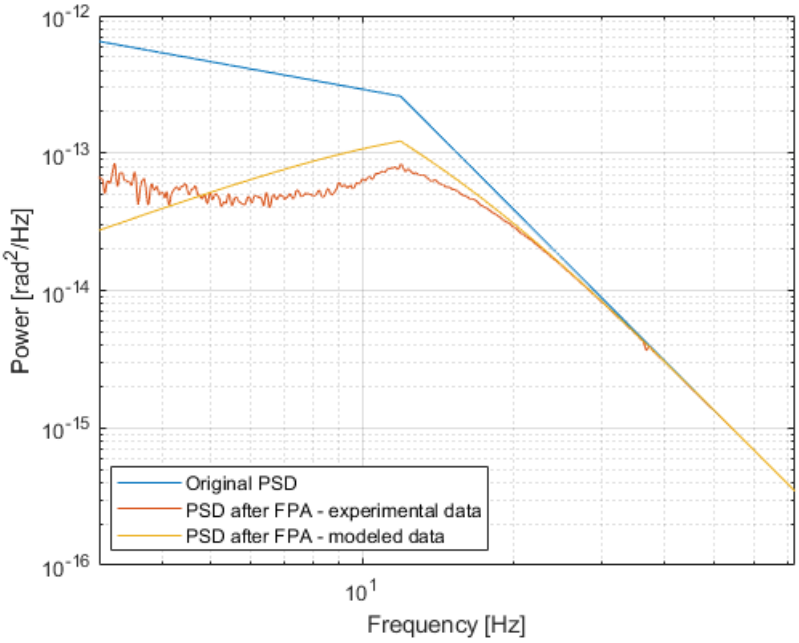

Figure 3.7: PSD or unaltered Tip-Tilt spectrum alongside propagated versions through model and experimental data.

Figure 3.7 indeed shows high-pass behaviour of the FPA. It can be observed that the model and experiment have some discrepancies, mostly in the lower frequency domain. Beyond 30Hz, the FPA does not remove significant amounts of energy, and the PSDs overlap. Hence, the dismissal of the model mismatch above $36Hz$ is considered justified. Lastly, the effect of the limited bandwidth of the FPA is not visible.

The total energy in the considered spectrum was computed with a Riemann sum and yielded the results shown in Table 3.3.

PSD	total energy [rad^2]
Glindemmann (unaltered)	$6.3599 \cdot 10^{-12}$
Analytical FPA	$1.5094 \cdot 10^{-12}$
Experimental FPA	$1.3537 \cdot 10^{-12}$

Table 3.3: Comparison of total disturbance energy in the original and propagated PSDs.

The total energy of the propagated PSDs differs $\approx 10\%$ and is attributed to the model fit and measurement quality in the lower frequency domain ($< 36Hz$). Discrepancies are emphasized by the logarithmic scale and squaring action of the absolute value.

The analytical spectrum is used to attain a conservative energy removal performance metric. The FPA from this thesis removes 76% of the tip-tilt disturbance energy presented in the observed frequency spectrum.

The actual performance is estimated to be slightly lower, however, as the FPA is not removing much energy in the higher frequency domain. Disturbance energy outside the $3 - 72.5Hz$domain is not included in the above energy comparison. The analysis was performed for a single axis, but the result can be applied to both axes of the FPA.

3.2.Discussion

This section discusses the limitations of the FPA revealed by the results, analysis, and observations.

Digital Image processing

The DIP toolchain is limited in sampling frequency due to latency in the processing of the full frames, a direct effect of not implementing a region of interest (ROI).

From requirement **FPA1-3-1A**, it is clear that the desired bandwidth is more than the required 1/10x of the sampling frequency for applying continuous control theory. With any increase in sampling frequency, the operational bandwidth will follow, making continuous control unreasonable. Therefore, discrete control theory is required. The theoretical bandwidth limit is 1/5x the sampling frequency [32, p.322]. The ideal bandwidth at $400Hz$ sampling of full frames is $80Hz$. Practically, with $72.5Hz$ sampling, the limit is at $14.5Hz$. However, with the desired characteristics presented in Section 2.2.4, a bandwidth of $8Hz$ was realized.

Another implication of the relatively low sampling frequency, as mentioned in Section 2.3.1, is the need for the lock-in amplifier to oversample the DIP return signal. This degrades the resolution close to the Nyquist frequency.

Measurement platform

Using the IR camera as the measurement platform has severe implications on the performance of the FPA. The IR camera used to track the spot has been considered a means to measure the true angular deflection of the optical axis. This choice was made because the optical sensors from the OIM102 mirror showed discrepancies between commanded and observed angular deflections in one of the axes, seen from the perspective of the camera. Using the IR camera as a calibration platform has led to the use of linear interpolation when determining the coefficients for conversions of command and readout voltage signals. Though the voice coil actuators in the FSM have a linearity of 1% over the range [4], there is a significant risk that coefficients were overfitted.

Overfitting effects may be observed in the open loop bode plot from Figure 3.2. Here, the gain plot for a large section of the relevant frequency spectrum is centered around $0dB$. Though this is a desirable gain that could indicate the OIM PID controller is working properly, it might also indicate bias in the signal conversion. Without an external measurement platform, it is hard to quantify the effect of the possible bias.

Finally, by matching the camera readings with the correction factors, the mistake in the optical setup is less visible in the data readings.

System requirement generation

As already specified in Section 2.1.1, the data detection circuit is not part of this thesis due to time constraints. This introduces a limitation of the FPA when it comes to requirement verification. All system requirements in Table 1.3 were based on literature and heritage. However, ultimately, the FPA design requirements flow from the application, in this case, acceptable angular deflections for SMF coupling, maximum allowable fade rate, and fade duration.

COG algorithm

The selected tracking algorithm for the FPA was COG, a weighted average based on intensity for each axis. This algorithm was primarily chosen because of its simplicity and low computational efforts directly related to latency. This computed average may coincide with max intensity, for Gaussian and plane wave this is the case as they are rotationally symmetric. However, for asymmetric atmosphere-induced speckle patterns, this assumption is no longer valid.

Different algorithms might be more appropriate, for instance, blob detection using thresholds, morphological filters (successive erosion and dilation [50]), and mathematical operations. This algorithm could be set up to select the local COG of the blob with the highest intensity.

Note that this algorithm was explored using the OpenCV[50] components within RTMaps. Unfortunately, however, it was found that processing introduced too much latency. This component was additionally only applicable to 8-bit/pixel images, lowering the resolution considerably. Lastly, it was

found that this off-the-shelf algorithm applied a Gaussian filter, essentially lowering the resolution even further.

Exploring new algorithms for spot tracking must be done with great care for penalties in both resolution and latency. For an operational FPA, it is therefore desirable to write another custom component for RTMaps.

MISO implementation
Ultimately, the FPA is designed for operations on MISO in order to facilitate FSOC downlink experiments. To this end, the FPA must be mounted on the telescope rear breadboard shown in Figure 1.1. A new characterization campaign is expected to highlight the influence of the telescope movement on the response and subsequent performance of the FPA.

It is hypothesised that the performance of the FPA will be worsened as a result of these additional mechanical loads and vibrations, these were not present in the lab campaign. These effects are expected to increase the disturbance power in the higher frequency domain ($> 30Hz$), which, as shown by Figure 3.6 and 3.7, is not well mitigated by the current implementation of the FPA.

Software implementation
From the results presented in Section 3.1.4, it becomes apparent that latency drives the loop frequency of the FPA its control systems. The rated performance of the individual components of the FPA, in fact, in all cases, is not met. This implies that the low loop speed can be attributed to the software implementation of the system, be it in both custom and off-the-shelf software suites.

In the past, latency was reduced by streamlining programming in RTMaps. For example, not polling every frame to retrieve the threshold in the ”properties” field of RTMaps. Instead, storing this value in memory during the ”birth” part of the component and later referring to it in the ”core” section. This particular intervention sped up the processing, no longer experiencing FIFO buffer overflows within the RTMaps environment.

Another example of latency mitigation through programming choices is found in the COG RTMaps component. Here, latency was mitigated by not evaluating the summing action of the weighted average if the pixel value was below the threshold. As most pixels of each frame are below the threshold, latency was reduced.

Latency mitigation programming campaigns may further increase the loop frequency. In these attempts, from the latency budget in Table 3.2, it is clear that the focus should be on the Grablink-RTMaps interface as its latency contribution is almost an order of magnitude bigger than all other contributors combined. A foreseen challenge is the callback mechanism currently imposed by the MultiCam driver. This mechanism currently has some stochastic properties in timing and is outside of direct timing control by the user.

4
Conclusion & Recommendations

This final chapter concludes this thesis. The requirements are checked for compliance, insights are presented, and recommendations for future research are laid out.

4.1.Conclusion

The mini optical ground Station (MISO) on top of the Aerospace Engineering Faculty of Delft - University of Technology aims to demonstrate free space optical communication (FSOC) related technology. An important segment within the FSOC toolchain, the fine pointing assembly (FPA), was designed, developed, and characterized in this thesis.

The objective of this design task:

Design, develop and characterize an opto-mechatronic integrated system to achieve Fine Pointing for MISO

The FPA for MISO was designed to remove disturbance energy from the atmospheric tip-tilt single-sided disturbance power spectral density (PSD). The design was centered around two uncoupled, parallel control systems, each mitigating either the tip or tilt per orthogonal axis. This was achieved using a fine steering mirror (FSM) as the actuator to steer the light equal but opposite to the disturbance. The FSM was to be commanded through a simple feedback controller that received its feedback signal from the Digital Image Processing toolchain, which is responsible for beam tracking. With the use of a beam splitter, part of the received light was used for disturbance mitigation, while the remaining light was intended for data detection but with tip-tilt disturbance energy removed.

A functional FPA was made from OIM102 FSM, Xenics Bobcat 320CL, RTMaps, bulk optics, and a dSPACE MicroLabBox. Figure 3.1 shows the integrated system in the lab environment. Compliance with customer and system requirements is established in Table 4.1 and 4.2, respectively.

Label	Summary	Compliance (Y/N)	Addressed in:
FPA1-1	In-house components	N	Section 2.1.2
FPA1-1A	Lab demonstration	Y	Section 2.1.2
FPA1-1B	Digital Image Processing	N	Section 3.1.4
FPA1-2	Modular design	Y	Section 2.1.3

Table 4.1: Customer requirements compliance matrix

Label	Performance parameter	Target value	Obtained value	Compliance (Y/N)	Addressed in:
FPA1-3	Facilitate fiber coupling	N.A.	N.A.	N	N.A.
FPA1-3-1	Reduce tip-tilt	N.A.	N.A.	N	N.A.
FPA1-3-1A	Cross-over bandwidth	$1kHz$	$8Hz$	N	Section 3.1.5
FPA1-3-1B	Reduce total tip-tilt disturbance energy visible in PSD	$> 0\%$	76%	Y	Section 3.1.5
FPA1-3-2	Tracking resolution	$< 5\mu rad$	$20\mu rad$	N	Section 3.1.3
FPA1-3-3	Angular acceptance range	$\pm 500\mu rad$	$\pm 0.25rad$	Y	Section 3.1.1

Table 4.2: System requirements compliance matrix.

The performance of the FPA for MISO is limited by latency originating in the interface between Frame Grabber and RTMaps. With a latency contribution of $0.014s$ of this interface, the control loop frequency is $72.5Hz$ rather than the desired $> 1kHz$. The FPA implementation performs within approximately 10% of the analytically predicted performance in terms of removed energy from the tip-tilt power spectrum. The current version of FPA removes roughly 75% of the tip-tilt disturbance energy.

Throughout the development process of the FPA covered in this thesis, several insights were gained.

- An integrated design of FPA cannot be dealt with as an isolated problem covering a single engineering domain. The FPA development of this thesis covered the following domains:
  - Control
  - Software
  - Mathematics
  - Optics
  - Mechatronics
  - Probability and statistics

  Although future iterations of this FPA design require specific activities, as discussed below in Section 4.2, all activities must be performed with the relation to these engineering domains in mind.
- The design of an FPA using the OIM102 FSM can be done under the assumption that the system is comprised of two independent single-input-single-output (SISO) systems, one for each respective axis.
- The achievable tracking resolution at a representative received optical power is determined by optical design and detector layout.
- Digital image processing, when using full-frame images, demands the application of discrete control theory as latency forces the design bandwidth to be within 10x the effective sampling frequency of the feedback signal.
- Performance estimates of the FPA, beyond its dynamic response, benefit from the comparison of Power Spectral Densities of the incoming beam before and after Tip-Tilt mitigation.

4.2.Recommendations

Figure 4.1 provides an overview of recommended activities for the FPA.

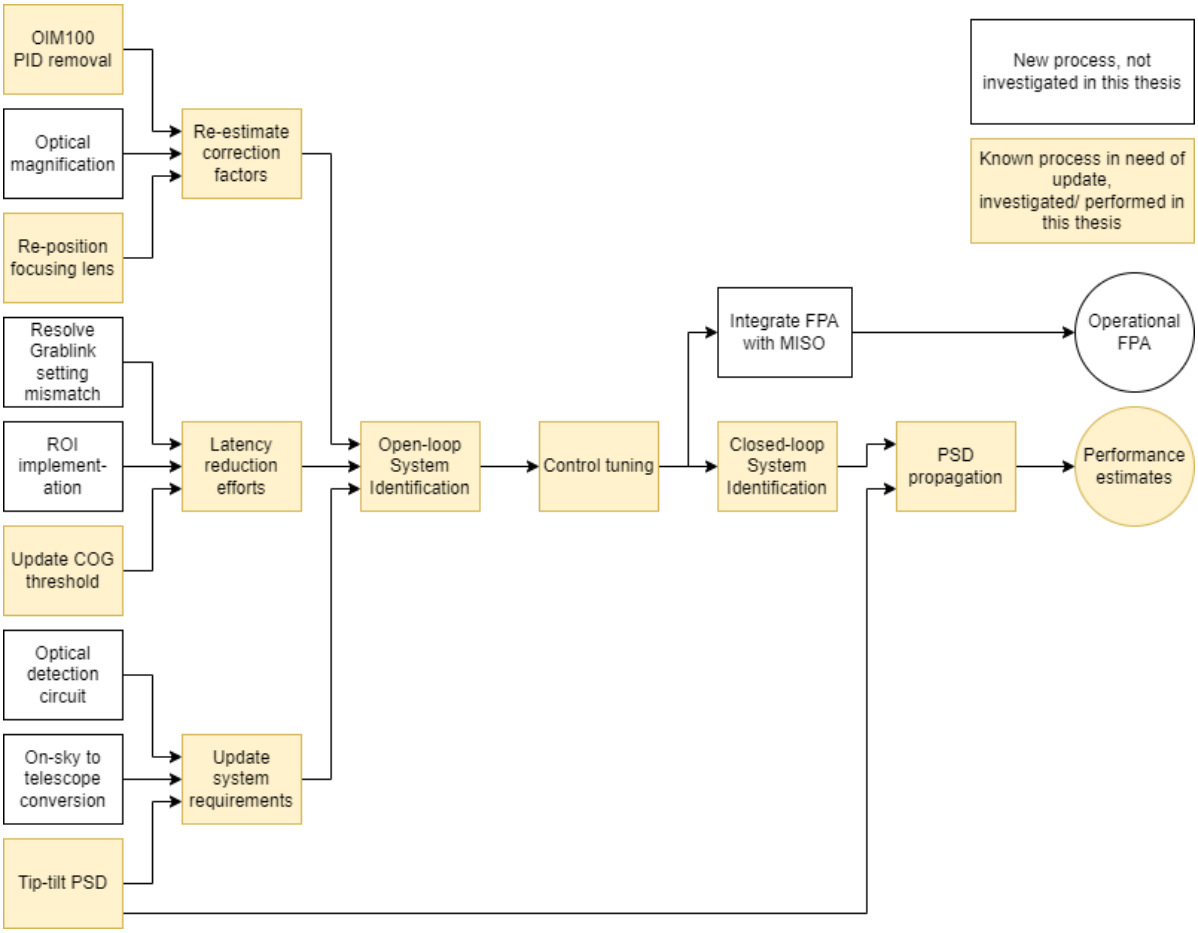

Figure 4.1: Workflow diagram of the recommended activities in future research.

1. **OIM PID controller removal:** Combining the OIM100 PID controller and its dynamic response with the design bandwidth violates standard rules for loop shaping of 2nd order mass-spring-damper systems [32, p.283]. The OIM PID needs removal to tune the controller properly. Note that the performance of the FPA will still be latency-limited. The PID controller was not removed in this study to reduce scheduling risk.

2. **Optical magnification:** Including an optical magnification stage can improve e the tracking resolution. An increase in focal length, given the same angular deflection, increases the linear displacement of the spot projection. When sticking to a full frame, a 50x magnification is recommended, this will however affect the overall footprint of the FPA on the breadboard.

3. **Re-position focusing lens:** Position focusing lens such that both FSM-A and the IR camera detector are placed at the focal distance.

4. **Resolve Grablink settings mismatch:** Change CAM file to reflect the correct mode of operation (RC mode[51]). Additionally, it is recommended to test the interface latency by measuring latency within RTMaps but with timestamped software triggers. Refer to the email conversation with Euresys (Project folder).

5. **ROI implementation:** Applying a region of interest (ROI) will require the transfer of less data per sampling interval into the Linux RAM, the main source of latency in the FPA. With ROI, the sampling frequency can go up to 10kHz[5]. Ultimately, the size of the ROI, and thereby the reduction in latency, is traded for angular resolution as the pixel pitch stays constant. Optical magnification to increase the resolution is also inversely proportional to the required size of the ROI.

6. **Update COG threshold:** Change the default value of the threshold within the COG component of RTMaps (already implemented).

7. **Optical detection circuit:** refer to Section 3.2 - System requirement generation.

8. **On-sky to telescope conversion:** refer to Section 3.2 - System requirement generation.

9. **Integrate FPA with MISO:** Section 3.2- MISO implementation

The activities presented in Figure 4.1 but not specified above are repetitions of process already covered by this thesis.

References

[1] *Nielsen's law of internet bandwidth*, https://www.nngroup.com/articles/law-of-bandwidth/, Accessed: May 9, 2023.

[2] A. Raj and A. Majumder, "Optical communication in space: Challenges and mitigation techniques," *IEEE Communications Surveys & Tutorials*, vol. 19, no. 1, pp. 57–96, 2019. DOI: 10.1109/COMST.2016.2603518.

[3] R. J. Noll, "Zernike polynomials and atmospheric turbulence∗," *J. Opt. Soc. Am.*, vol. 66, no. 3, pp. 207–211, Mar. 1976. DOI: 10.1364/JOSA.66.000207.

[4] "Oim102-two inch fsm," Optics In Motion LLC, 4223 Rutgers Ave, Long Beach, CA 90808, Tech. Rep., Nov. 2008. [Online]. Available: https://opticsinmotion.org/wp-content/uploads/2019/09/OIM102-Specification-sheet-11-25-08.pdf.

[5] *Bobcat 320 series*, https://www.exosens.com/products/bobcat-320-series, Accessed: March 22, 2024.

[6] A. Jahid, M. H. Alsharif, and T. J. Hall, "A contemporary survey on free space optical communication: Potentials, technical challenges, recent advances and research direction," *Journal of Network and Computer Applications*, vol. 200, p. 103 311, 2022. DOI: 10.1016/j.jnca.2021.103311.

[7] *Starlink*, https://www.starlink.com/, Accessed: April 15, 2024.

[8] *Viasat*, https://www.viasat.com/, Accessed: April 15, 2024.

[9] *Hughens*, https://www.hughesnet.com/, Accessed: April 15, 2024.

[10] *Laser satellite communications group*, https://www.tudelft.nl/lr/laser-satellite-communications, Accessed: April 15, 2024.

[11] *Alluna ritchey-chrétien telescopes*, http://www.alluna-optics.com/Ritchey-Chretien-Telescope.html, Accessed: February 2, 2024.

[12] *L-500 direct drive mount*, https://www.planewave.eu/en/products/mount/l-500-direct-drive-mount, Accessed: February 2, 2024.

[13] A. Malik and P. Singh, "Free space optics: Current applications and future challenges," *International Journal of Optics*, vol. 2015, 2015. DOI: 10.1155/2015/945483.

[14] N. Pachler, B. del Portillo Barrios Inigo, and E. C. B. Cameron, "An updated comparison of four low earth orbit satellite constellation systems to provide global broadband," Jun. 2021, pp. 1–7. DOI: 10.1109/ICCWorkshops50388.2021.9473799.

[15] M. Aldecocea, M., P. Piron, *et al.*, "Opto-thermo-mechanical phenomena in satellite free-space optical communications: Survey and challenges," *Optical Engineering*, vol. 63, no. 4, pp. 1–29, 2023. DOI: 10.1117/1.OE.63.4.041206.

[16] E. Perez, M. Bailly, and J. M. Pairot, "Pointing acquisition and tracking system for silex inter satellite optical link," in *Acquisition, Tracking, and Pointing III*, S. Gowrinathan, Ed., International Society for Optics and Photonics, vol. 1111, SPIE, 1989, pp. 277–288. DOI: 10.1117/12.977988.

[17] S. Piazzolla, W. T. Roberts, . Kovalik, *et al.*, "Ground station for terabyte infrared delivery (tbird)," in *Free-Space Laser Communications XXXV*, H. Hemmati and B. S. Robinson, Eds., International Society for Optics and Photonics, vol. 12413, SPIE, 2023, p. 1 241 311. DOI: 10.1117/12.2655123.

[18] A. Biswas, M. Srinivasan, K. Andrews, *et al.*, "Deep space optical communications technology demonstration," in *Free-Space Laser Communications XXXVI*, H. Hemmati and B. S. Robinson, Eds., International Society for Optics and Photonics, vol. 12877, SPIE, 2024, p. 1 287 706. DOI: 10.1117/12.3001750.

[19] M. Krynitz, C. Heeseb, M. Knoppc, K. Schulzb, and H. Hennigera, "The european optical nucleus network," in *16th International Conference on Space Operations*, International Society for Optics and Photonics, vol. 12877, International Astronautical Federation, 2021, p. 8x1477.

[20] S. Maroquin, "Evaluating the improvement of atmospheric aberration corrections with the use of adaptive optics: Enabling inter-island communication through quantum encrypted optical communications," Delft University of Technology - Aerospace Engineering, Delft, Tech. Rep., Aug. 2023. [Online]. Available: https://repository.tudelft.nl/islandora/object/uuid%3Ad4bd6483-884d-4da8-9f14-156f4effb0ff?collection=education.

[21] H. Komatsu, S. Ohta, H. Yamazoe, *et al.*, "The pointing performance of the optical communication terminal, soliss in the experimentation of bidirectional laser communication with an optical ground station," in *Free-Space Laser Communications XXXIII*, H. Hemmati and D. M. Boroson, Eds., International Society for Optics and Photonics, vol. 11678, SPIE, 2021, 116780F. DOI: 10.1117/12.2577067.

[22] F. Moll, A. Shrestha, and C. Fuchs, "Ground stations for aeronautical and space laser communications at german aerospace center," in *Unmanned/Unattended Sensors and Sensor Networks XI; and Advanced Free-Space Optical Communication Techniques and Applications*, E. M. Carapezza, P. G. Datskos, C. Tsamis, L. Laycock, and H. J. White, Eds., International Society for Optics and Photonics, vol. 9647, SPIE, 2015, p. 96470I. DOI: 10.1117/12.2194093.

[23] F. Bennet, K. Ferguson, K. Grant, E. Kruzins, N. Rattenbury, and S. Schediwy, "An australia/new zealand optical communications ground station network for next generation satellite communications," in *Free-Space Laser Communications XXXII*, H. Hemmati and D. M. Boroson, Eds., International Society for Optics and Photonics, vol. 11272, SPIE, 2020, p. 1 127 202. DOI: 10.1117/12.2545305.

[24] R. C. Johnson, J. M. Wicker, A. Lin, *et al.*, "Development and deployment of remotely operable optical communication terminals," in *36th Annual Small Satellite Conference*, The Aerospace Corporation, 2022.

[25] E. P. Goodwin and J. C. Wyant, *Field Guide to Interferometric Optical Testing*. Bellingham, Washington: SPIE Press, Sep. 2006.

[26] A. Glindemann, "Relevant parameters for tip-tilt systems on large telescopes," *Publications of the Astronomical Society of the Pacific*, vol. 109, no. 736, pp. 682–687, 1997. DOI: 10.1086/133932.

[27] D. Garner, *Optical fiber 101 single mode fiber - part 2 using single mode fiber*, Webinar, Nov. 2021. [Online]. Available: https://www.youtube.com/watch?v=HvJeXakc8Kc.

[28] Y. Takayama, T. Jono, M. Toyoshima, *et al.*, "Tracking and pointing characteristics of oicets optical terminal in communication demonstrations with ground stations," *Proceedings of SPIE*, vol. 6457, p. 645 707, 2007. DOI: 10.1117/12.708417.

[29] D. Gray, *How to make a pointxp model*, Webinar, Aug. 2019. [Online]. Available: https://www.youtube.com/watch?v=s_vQZSa9rz8.

[30] *Microlabbox - recommended starting points*, https://www.dspace.com/en/pub/home/support/documentation.cfm?hlevel2=MicroLabBox&hlevel1=StartPageHardware, Accessed: October 19, 2023.

[31] *User's manual oim100 series fsm models oim101, oim102, oim102.3*, Optics In Motion, Oct. 2008.

[32] R. M. Schmidt, G. Schitter, A. Rankers, and J. van Eijk, *The Design of High Performance Mechatronics - High-Tech Functionality by Multidisciplinary System Integration*, 3rd revised ed. Nieuwe Hemweg 6b 1013 BG Amsterdam, The Netherlands: Delft University Press, 2020.

[33] "Oim5001-small one inch fsm," Optics In Motion LLC, 4223 Rutgers Ave, Long Beach, CA 90808, Tech. Rep., Dec. 2013. [Online]. Available: https://opticsinmotion.org/wp-content/uploads/2019/09/OIM5001-Specification-Sheet-12-23-2013.pdf.

[34] *Small oem fast steering mirror controller oimc101a*, Rev. B, Optics In Motion, Apr. 2021.

[35] *Series 2200 multichannel programmable dc power supplies - user's manual*, Rev. C, Keithley, Dec. 2013.

[36] *Specifications of the camera link interface standard for digital cameras and frame grabbers*, http://www.imagelabs.com/wp-content/uploads/2010/10/CameraLink5.pdf, Accessed: April 16, 2024.

[37] *Grablink full*, https://www.euresys.com/en/Products/Frame-Grabbers/Grablink-series/Grablink-Full, Accessed: May 11, 2024.

[38] *Developing real-time multisensor applications with rtmaps™*, https://intempora.com/products/rtmaps/, Accessed: October 2, 2023.

[39] *Rtmaps component lifecycle*, https://support.intempora.com/hc/en-us/articles/360007394594-RTMaps-Component-Lifecycle, Accessed: October 2, 2023.

[40] G. Schitter, *Vu 376.045 - messtechnik_09 zeit und frequenzmessung*, Lecture slides, Mar. 2016.

[41] F. Dekking, C. Kraaikamp, H. Lopuhaä, and L. Meester, *A Modern Introduction to Probability and Statistics - Understanding Why and How*. Delft, The Netherlands: Springer, 2005.

[42] *Rtmaps sdk api reference - rtmaps v4.10.4*, Intempora, Dec. 2022.

[43] *Timestamp and time of issue*, https://support.intempora.com/hc/en-us/articles/115002840494-Timestamp-and-Time-of-issue, Accessed: May 11, 2024.

[44] R. Hoogeveen, *Ae4880 - course on space detector systems*, Lecture slides, Mar. 2022.

[45] *User manual bobcat-640-gige&cl camera & bobcat-320-gige&cl camera & bobcat+-320-gige camera, eng-2012-umn020-r012*, Xenics, Sep. 2021.

[46] L. Meester, *Wi4525tu- monte carlo simulations and stochastic processes - lecture 4*, Lecture slides, Sep. 2023.

[47] E. Csencsics, R. Saathof, and G. Schitter, "Design of a dual-tone controller for lissajous-based scanning of fast steering mirrors," in *2016 American Control Conference (ACC)*, 2016, pp. 461–466. DOI: 10.1109/ACC.2016.7524957.

[48] A. Biswas, M. Srinivasan, K. Andrews, *et al.*, "Deep space optical communications technology demonstration," in *Free-Space Laser Communications XXXVI*, H. Hemmati and B. S. Robinson, Eds., International Society for Optics and Photonics, vol. 12877, SPIE, 2024, p. 1 287 706. DOI: 10.1117/12.3001750.

[49] T. Riel, R. Saathof, A. Katalenic, and G. Schitter, "Noise analysis and improvement of a permanent magnet synchronous motor by dynamic error budgeting," *Mikroniek*, vol. 51, no. 2, pp. 5–12, 2016. DOI: 10.1016/j.ifacol.2016.10.578.

[50] *Morphological transformations*, https://docs.opencv.org/3.4/d9/d61/tutorial_py_morphological_ops.html, Accessed: October 17, 2023.

[51] *Area-scan operational modes*, https://documentation.euresys.com/Products/MULTICAM/MULTICAM/Content/03_MultiCam/Multicam_User_Guide/area-scan-operational-modes.htm, Accessed: March 18, 2024.

[52] D. Poncet, S. Glynn, and F. Heine, "Hosting the first edrs payload," in *International Conference on Space Optics — ICSO 2014*, Z. Sodnik, B. Cugny, and N. Karafolas, Eds., International Society for Optics and Photonics, SPIE, 2017, p. 105630D. DOI: 10.1117/12.2304091.

[53] J. M. Perdigues, Z. Sodnik, H. Hauschildt, *et al.*, "The esa's optical ground station for the edrs-a lct in-orbit test campaign: Upgrades and test results," in *International Conference on Space Optics — ICSO 2016*, B. Cugny, N. Karafolas, and Z. Sodnik, Eds., International Society for Optics and Photonics, vol. 10562, SPIE, 2017, p. 105622V. DOI: 10.1117/12.2296098.

[54] Y. Koyama, M. Toyoshima, Y. Takayama, *et al.*, "Sota: Small optical transponder for micro-satellite," in *2011 International Conference on Space Optical Systems and Applications (ICSOS)*, vol. 10562, 2011, pp. 97–101. DOI: 10.1109/ICSOS.2011.5783720.

[55] H. Takenaka, Y. Koyama, M. Akioka, *et al.*, "In-orbit verification of small optical transponder (sota): Evaluation of satellite-to-ground laser communication links," in *Free-Space Laser Communication and Atmospheric Propagation XXVIII*, H. Hemmati and D. M. Boroson, Eds., International Society for Optics and Photonics, vol. 9739, SPIE, 2016, p. 973 903. DOI: 10.1117/12.2214461.

[56] D. Giggenbach, C. Fuchs, C. Schmidt, *et al.*, “Downlink communication experiments with osirisv1 laser terminal onboard flying laptop satellite,” *Applied Optics*, vol. 61, no. 8, pp. 1938–1946, 2022. DOI: 10.1364/AO.446771.

[57] C. Fuchs, C. Schmidt, J. Keim, *et al.*, “Update on DLR’s OSIRIS program and first results of OSIRISv1 on Flying Laptop,” in *Free-Space Laser Communications XXXI*, H. Hemmati and D. M. Boroson, Eds., International Society for Optics and Photonics, vol. 10910, SPIE, 2019, 109100S. DOI: 10.1117/12.2514349.

[58] H. Komatsu, S. Ohta, H. Yamazoe, *et al.*, “In-orbit experimental architecture design of bi-directional communication with a small optical communication terminal attached on ISS and an optical ground station,” in *Free-Space Laser Communications XXXII*, H. Hemmati and D. M. Boroson, Eds., International Society for Optics and Photonics, vol. 11272, SPIE, 2020, p. 112720C. DOI: 10.1117/12.2551257.

[59] P. Serra, O. Cierny, R. Diez, *et al.*, “Optical communications crosslink payload prototype development for the cubesat laser infrared crosslink (click) mission,” in *33rd Annual AIAA/USU Conference on Small Satellites*, 2019.

[60] C. Payne, A. Aguilar, D. Barnes, *et al.*, “Integration and testing of the nanosatellite optical downlink experiment,” in *32nd Annual AIAA/USU Conference on Small Satellites*, 2018.

[61] C. M. Schieler, K. M. Riesing, A. J. Horvath, *et al.*, “200 Gbps TBIRD CubeSat downlink: pre-flight test results,” in *Free-Space Laser Communications XXXIV*, H. Hemmati and B. S. Robinson, Eds., International Society for Optics and Photonics, vol. 11993, SPIE, 2022, 119930P. DOI: 10.1117/12.2615321.

[62] T. S. Rose, D. W. Rowen, S. D. LaLumondiere, *et al.*, “Optical communications downlink from a low-earth orbiting 1.5u cubesat,” *Opt. Express*, vol. 27, no. 17, pp. 24 382–24 392, Aug. 2019. DOI: 10.1364/OE.27.024382.

[63] H. Tomio, T. Kuwahara, S. Fujita, *et al.*, “Assembly and integration of optical downlink terminal VSOTA on microsatellite RISESAT,” in *International Conference on Space Optics — ICSO 2018*, Z. Sodnik, N. Karafolas, and B. Cugny, Eds., International Society for Optics and Photonics, vol. 11180, SPIE, 2019, 111805Z. DOI: 10.1117/12.2536134.

[64] T. Kuwahara, K. Yoshida, Y. Tomioka, *et al.*, “Laser data downlink system of micro-satellite risesat,” in *27th Annual AIAA/USU Conference on Small Satellites*, 2013.

[65] *Cubecat datasheet*, AAC Clyde Space, Nov. 2021. [Online]. Available: https://www.aac-clyde.space/wp-content/uploads/2021/10/CUBECAT.pdf.

[66] T. Jono, K. Nakagawa, Y. Suzuki, and A. Yamamoto, “Optical communications system of oicets,” in *16th International Communications Satellite Systems Conference*, American Institute of Aeronautics and Astronautics, 1996, pp. 793–801. DOI: 10.2514/6.1996-1079.

[67] K. Nakagawa and A. Yamamoto, “Engineering model test of LUCE (Laser Utilizing Communications Equipment),” in *Free-Space Laser Communication Technologies VIII*, G. S. Mecherle, Ed., International Society for Optics and Photonics, vol. 2699, SPIE, 1996, pp. 114–120. DOI: 10.1117/12.238408.

[68] T. Jono, Y. Takayama, N. Kura, *et al.*, “OICETS on-orbit laser communication experiments,” in *Free-Space Laser Communication Technologies XVIII*, G. S. Mecherle, Ed., International Society for Optics and Photonics, vol. 6105, SPIE, 2006, p. 610 503. DOI: 10.1117/12.673751.

A
Additional results

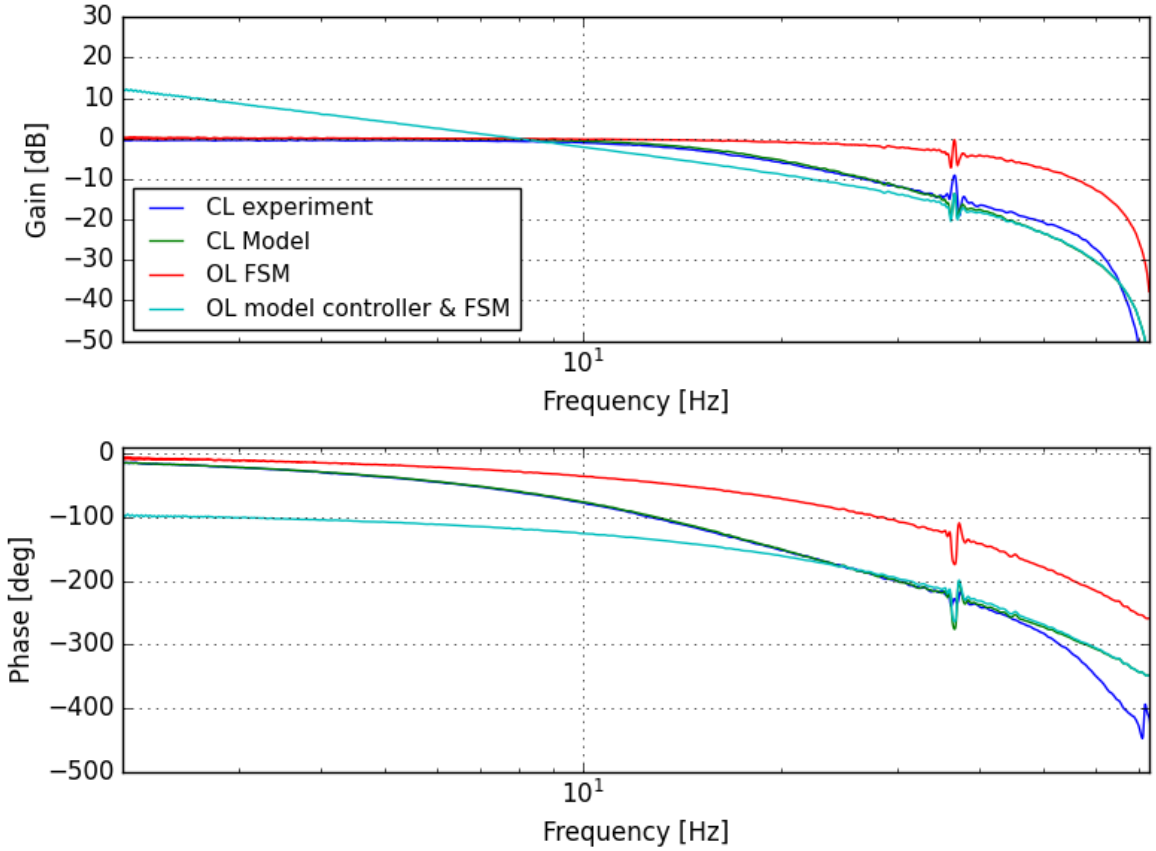

Figure A.1: X axis Bode plot of FPA in open-loop and closed-loop.

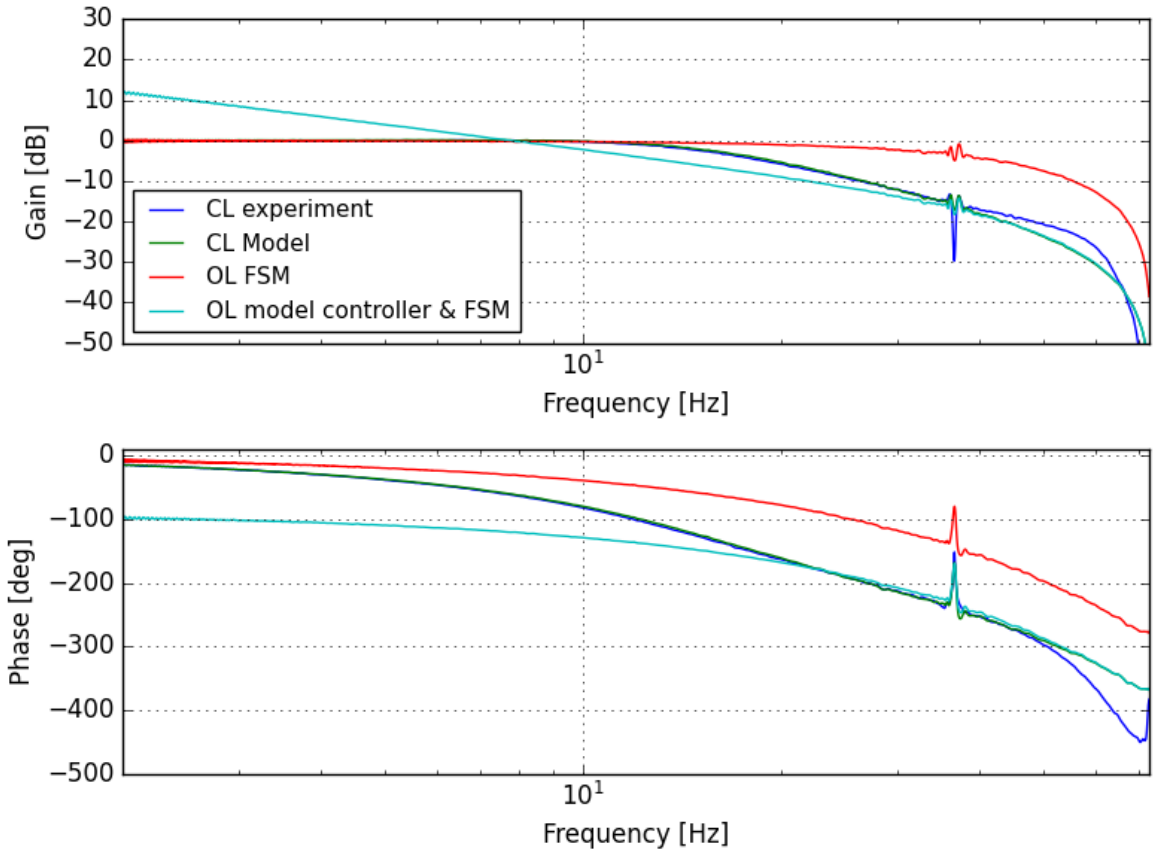

Figure A.2: Y axis Bode plot of FPA in open-loop and closed-loop.

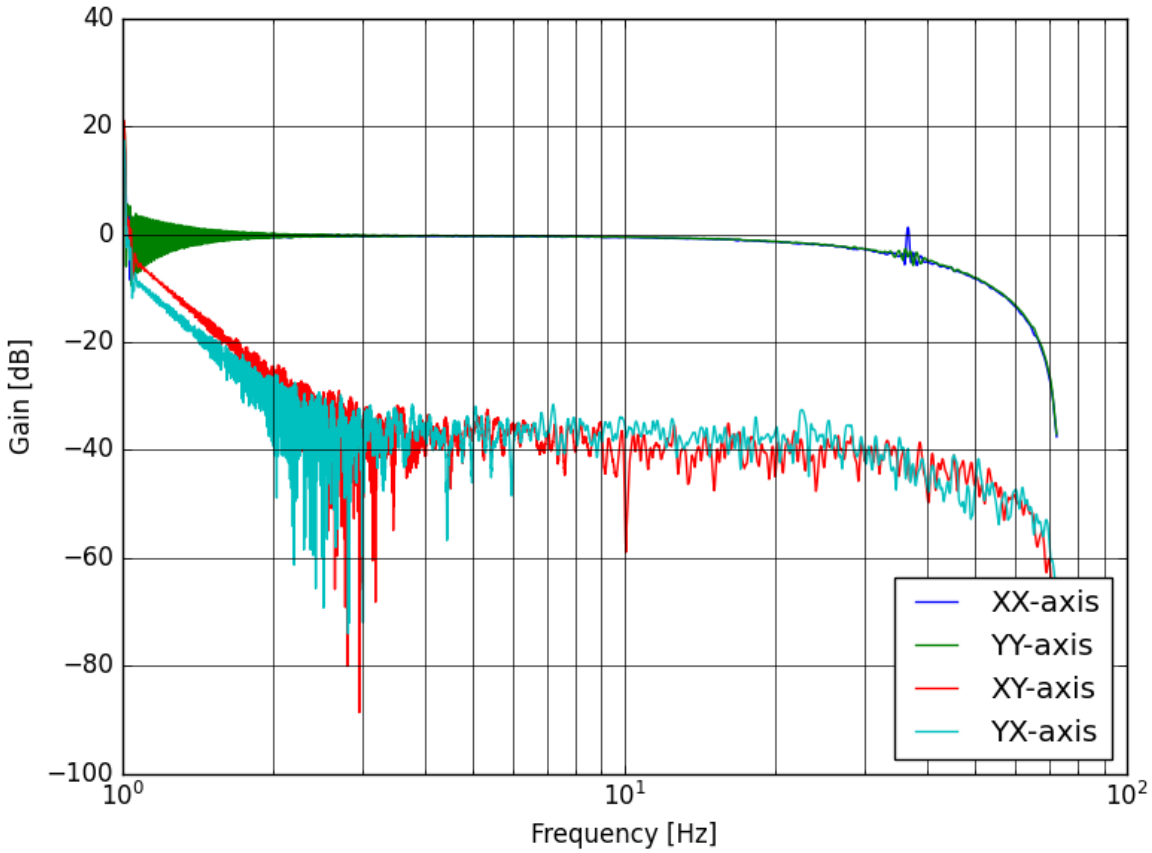

Figure A.3: Cross coupling FSMB (OIM 5001)

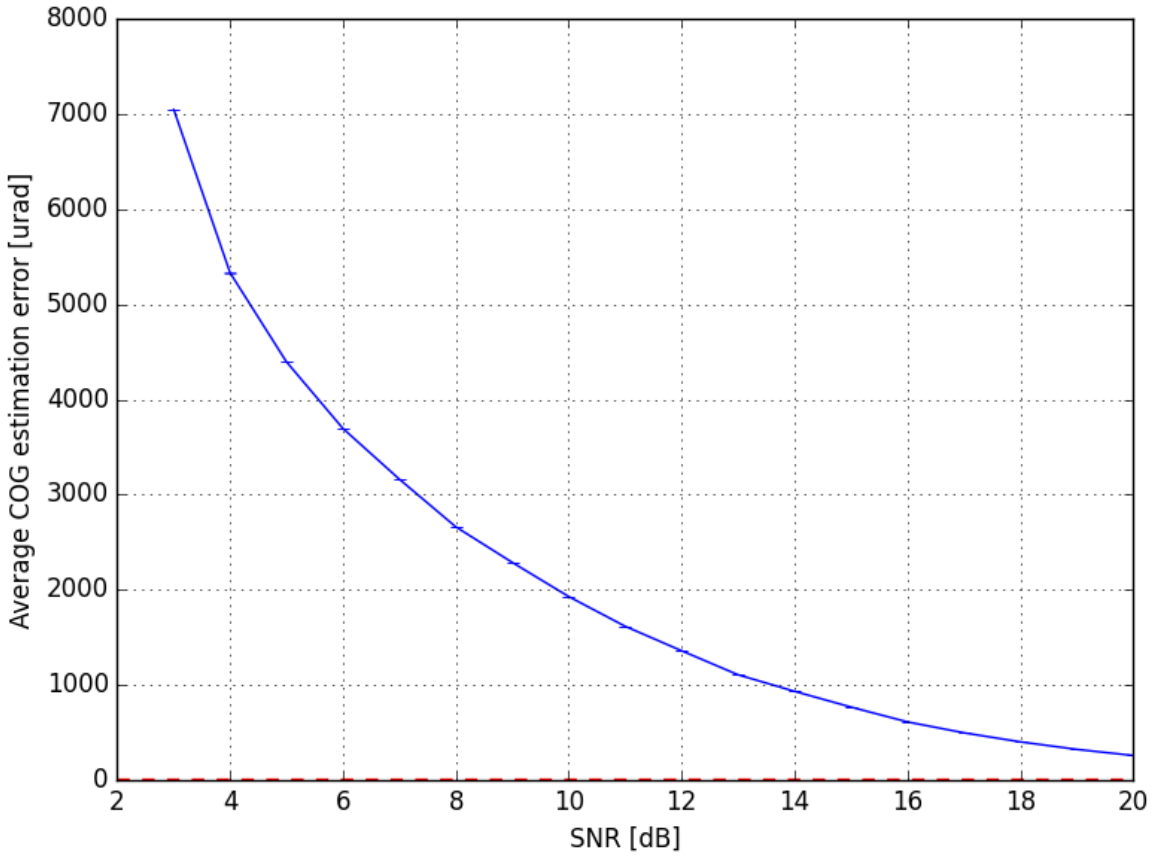

Figure A.4: Simulated camera resolution at various SNR values, threshold at 500 ADU after bias removal.

B
System Engineering diagrams

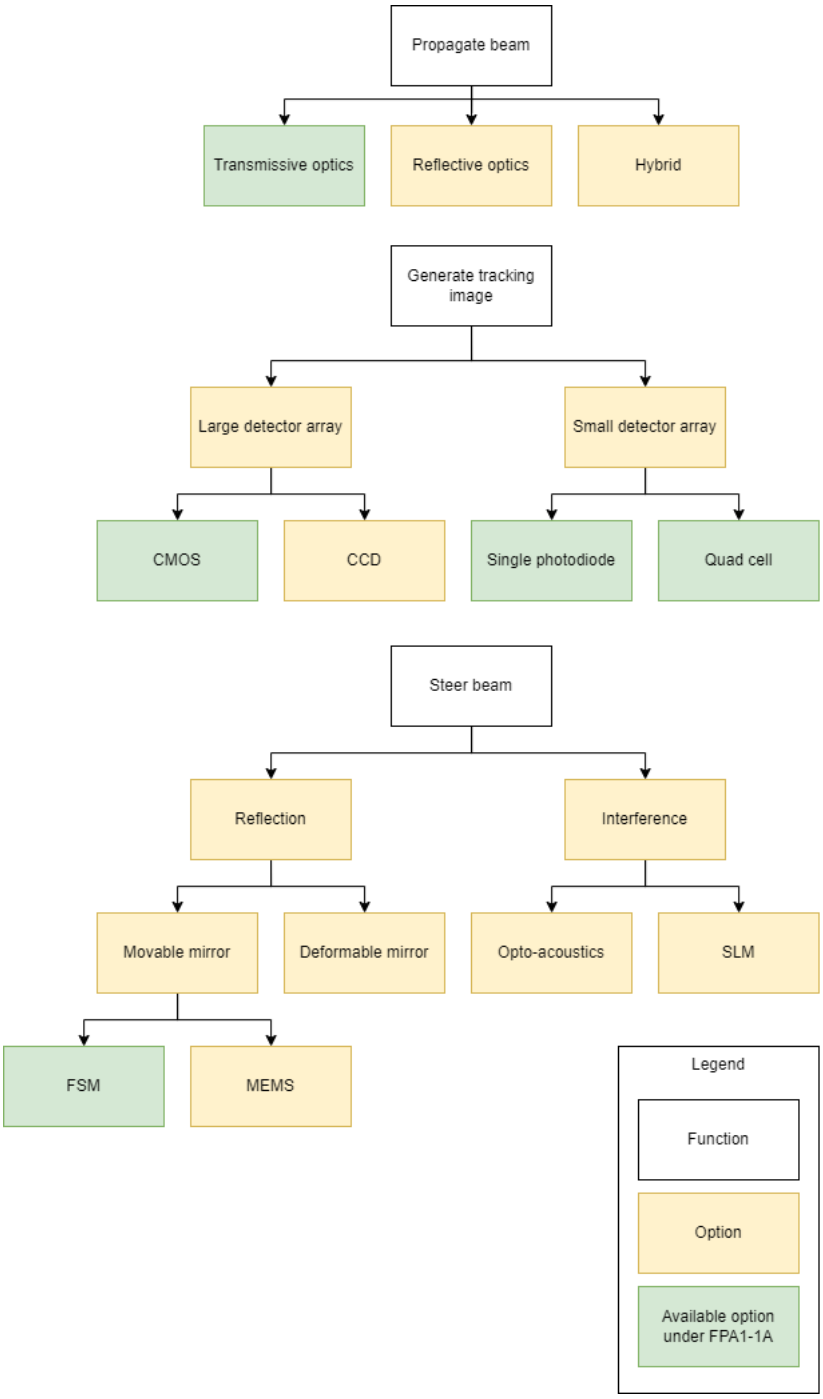

Figure B.1: Design option trees of main functions within FPA.

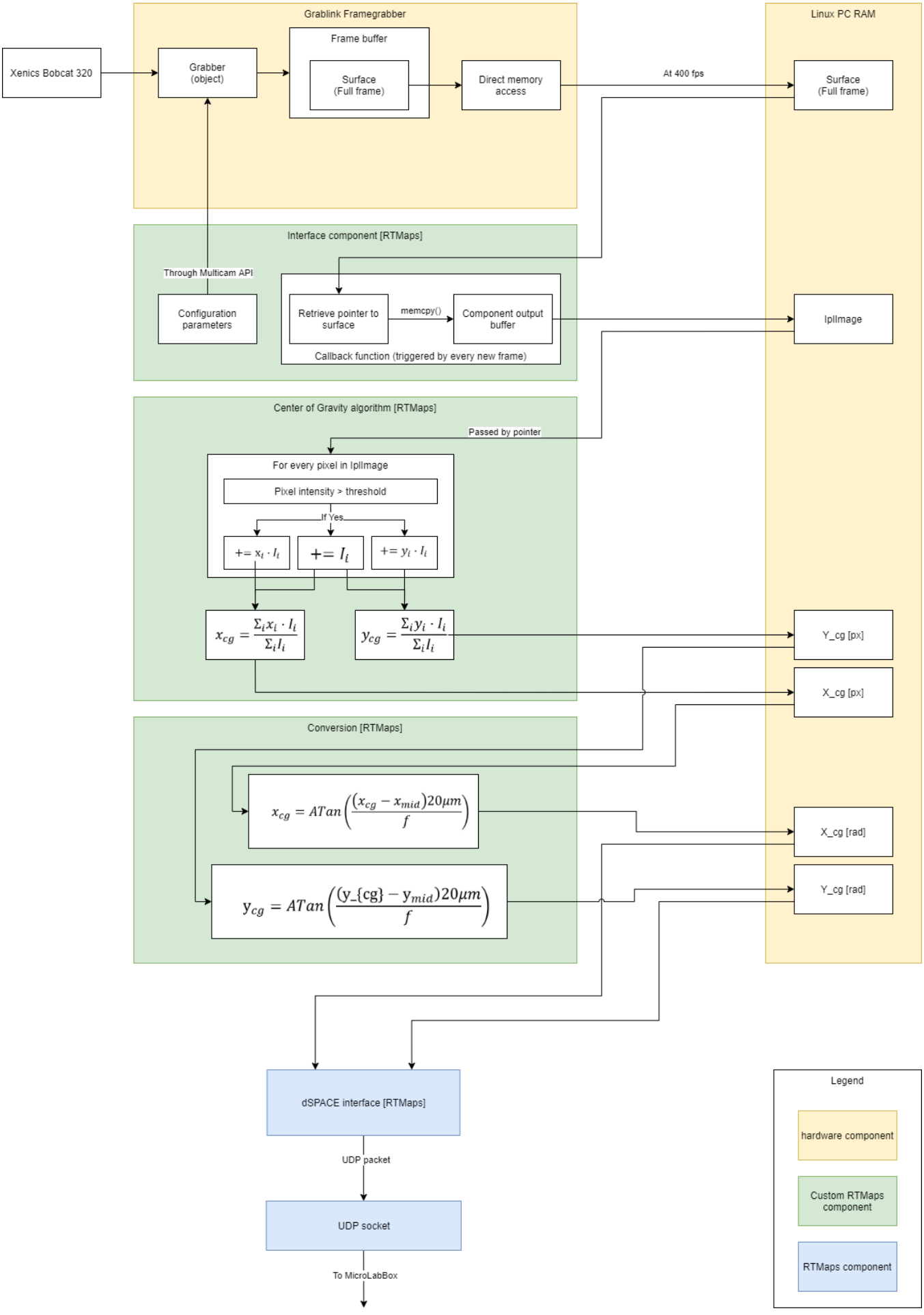

Figure B.2: Image Processing toolchain flowchart

C
Component Specifications

OIM102 - Optics In Motion		
Property	Quantity	Unit
Usable aperture	4.064	cm
Mechanical range	$\pm$ 1.5	$^{\circ}$
Pointing resolution	$\leq$2	μrad
Specified bandwidth (3dB)	750	Hz
Linearity	1%	-
Actuators	Voice coil (push-pull configuration)	-
Sensors	Optical (build in)	-

Table C.1: Specifications of the OIM102[4]

OIM5001 - Optics In Motion		
Property	Quantity	Unit
Usable aperture	2.3876	cm
Mechanical range	$\pm$ 3.0	$^{\circ}$
Pointing resolution	$\leq$1.2	μrad
Specified bandwidth (3dB)	850	Hz
Linearity	2%	-
Actuators	Voice coil (push-pull configuration)	-
Sensors	Optical (build in)	-

Table C.2: Specifications of the OIM5001[33]

Bobcat 320-CL - Xenics		
Detector type	CMOS	-
Material	InGaAs	-
Spectral band	900-1700	nm
ROIC topology	CTIA	-
Detector size	320x256	Px
Pixel pitch	20	μm
Full well (high gain)	125000	e-
QE	0.8	-
Bits per pixel	14	-
Max frame rate (full frame)	400	Hz
Digital output format	CameraLink (16 Bit)	-

Table C.3: Specifications of the Xenics Bobcat 320-CL[5]

Component	Part-number	Quantity
Optical components		
Laser diode	LDM1550	1
Neutral Density filters	NEK40A, NEK20A, NEK02A	1
2” flat aluminum mirror	ME2-G01	1
Bi-convex 100mm lens	LB1630	3
1” FSM	OIM5001	1
2” FSM	OIM102	1
Beam splitter 50:50	CCM1-BS015/M	1
supporting components		
1” mount	LMR1	1
Kinematic 2” mount	KM200	4
Laser mount	C11513/M	1
Rail 75mm	RLA75/M	2
Rail 150mm	RLA150/M	1
Clamping fork	CF125	4
Post holders	PH40E/M	3
Posts	various 50mm& 75mm	11
Spacers	various	11
Breadboard (metric)	700x450 mm	1

Table C.4: Components used in the optical setup of the FPA. Note laser alignment irises are not included but visible photographs.

D
Heritage database

Table D.1: Database of FSOC terminals from heritage.

Instrument	Platform	Mass [kg]	wavelength [nm]	Modulation	Functionality (Tx/Rx or both)	Mono-static/ Bi-static	Coarse pointing	Fine pointing	Reference
EDRS	Eutelsat-9B	35	1064	BPSK	Tx & Rx	Mono-static	Gimbal (CPA)	Tracking sensor + FSM	[52], [53]
SOTA	SOCRATES	5.9	1543 (Tx) 1064 (Rx)	OOK	Tx & Rx	Mono-static	Gimbal (CPA)	Quadcell + FSM	[54], [55]
OSIRIS V1	Flying laptop	1.3	1550	OOK	Tx	N.A.	Body pointing	Tracking sensor + tip-tilt mirror	[56]
OSIRIS V2	BiROS	1.65	1550	OOK	Tx	N.A.	Body pointing	Tracking sensor feedback to ADCS	[57]
SOLISS	ISS	9.8	1565 (Rx) 1550 (Tx)	OOK	Tx & Rx	Bi-static	Gimbal (CPA)	Quadcell + FSM	[58]
CLICK B/C	CLICK	1.5	1537 (Tx) 1563(Rx)	PPM	Tx & Rx	Mono-static	Body pointing	Quadcell + FSM (mems)	[59]
NODE	Did not fly		1550	PPM	Tx	N.A.	Body pointing	Quadcell + FSM (beacon)	[60]
TBIRD	PDT-3	3	1550	QPSK	Tx & Rx	Bi-static	Body pointing	PIN detector (feedback to ADCS)	[61]
OCSD-B&C	AeroCube-7	2.3	1064	OOK	Tx	N.A.	Body Pointing	N.A.	[62]
VSOTA	RISESAT	1	980 (Rx) 1550 (Tx)	OOK/PPM	Tx & Rx	Bi-static	Body Pointing	N.A.	[63], [64]
OSIRIS4CubeSat	PIXL-1	0.4	1550	OOK	Tx	N.A.	Body Pointing	Quadcell + FSM (beacon)	[57]
CubeCat	NORSAT-TD	1.33	1550	OOK	Tx & Rx	Unkown	Unknown	Unknown	[65]
LUCE	OICETS	140	819(Tx) 847 (Rx)	PPM(Tx) NRZ(Rx)	Tx & Rx	Mono-static	Gimbal (CPA)	CCD + FSM	[66], [67], [68]

Table D.2: Database of OGS from heritage.

Ground station name	organisation	location	wavelength band-width	residual pointing error [μrad]	Year (first light)	Aperture [cm]	operational?	Fine pointing	Feedback sensor	Correction bandwidth	Source
OCTL	JPL	Wrightwood	1064 and 1550	9.7	Not avail-able	100	Y	Adaptive optics	Xenics Cheetah	20kHz	[17]
DSS-13	JPL	Goldstone	1065 and 1550	<1	2023	130	Y	FSM (piezo electric)	Photon counting camera	15kHz	[18]
Unknown	EONN	Nemea	1529-1569	<24.2	2021	50	Y	Not available	Not available	Not available	[19]
Unknown	EONN	Almeria	1529-1569	<48.5	2022	60	Y	Not available	Not available	Not available	[19]
Unknown	EONN	Tenerife	1529.5-1568	<+-500	2021	80	Y	Deformable mirror (AO)	Wavefront sensor	Not available	[19],[20]
unknown	NICT(japan)	Tokyo	1550 Tx 1565 Rx	39.2	2019	100	Y	Fine pointing mechanism	Quadrant detector	90Hz	[21]
OGS-OP	DLR	Oberpfaffenhofen	Not avail-able	Not avail-able	2006	40	Y	FSM	NFOV camera (near infrared	Not available	[22]
TOGS	DLR	N.A.	Not avail-able	TBD	Under devel-opment	60	Planned	Not present	NFOV camera (near infrared	Not available	[22]
AOGSN	Australia-New Zealand	Network, vari-ous locations	1065 and 1550	TBD	Under devel-opment	50-70	Planned	Deformable mirror (AO)	Shack-Hartmann wavefront sensor	>1.5kHz	[23]
Unknown	The Aerospace cooporation	El Segundo (US)	1064	40	2019	40	Y	Not present	Xenics InGaAs camera array	Not available	[24]